Investigation of the existence and expected mass of a companion black hole for Sagittarius A*

Master's thesis

Written by *Charlotte Cramer Kristensen*

February 25, 2022

Supervised by

Prof. Anja C. Andersen

University of Copenhagen

NAME OF FACULTY: SCIENCE

NAME OF INSTITUTE: Niels Bohr Institute

AUTHOR(S):   Charlotte Cramer Kristensen

EMAIL: charlotteck@live.dk

TITLE AND SUBTITLE: Investigation of the existence and expected
                     mass of a companion black hole for Sagittarius
                     A*

SUPERVISOR(S):   Prof. Anja C. Andersen

HANDED IN: 25.02.2022

DEFENDED: 15.03.2022

NAME: Charlotte Cramer Kristensen

SIGNATURE

DATE: 25.02.2022

Acknowledgement

First and foremost, I would like to thank my supervisor Professor Anja C. Andersen for her guidance and support throughout the entire process of working on this thesis. I am very grateful for all of your ideas and patience, and it has been a pleasure working with you. A special thanks to my dear friend, Thea Quistgaard for the support and help with the project and in life. Thank you for your patience, help and good laughs when needed.

I would also like to thank my partner in crime writing my bachelor project, Anna T. Åkesson. Without you, I would not have any data to use for further work. In addition, I would like to send my appreciation to my loving and supporting friends, especially Felicia, Emilie, Jonas and Frederik.

Finally, I will send my thoughts and appreciation to my late mother, Susy. Thank you for your love, support and teaching me that anything is possible if you never give up.

Abstract

Binary systems is a well known phenomenon in the Universe. This thesis has investigated the possibility of the supermassive black hole, Sagittarius A*, in the center of the Milky Way being part of a binary system with a second black hole. In order to obtain knowledge of the companion black hole, it has been assumed that the two black holes are part of a triple body system with a star as the third body. Using this assumption, the Konzai-Lidov mechanism has been implemented in order to obtain an upper limit for the mass of the companion black hole. Previous work by Naoz et al. (2020) presented the opportunity of a companion black hole with a mass that does not exceed 10^5 M$_\odot$ with a semi-major axis greater than 170 AU for a circular orbit. This maximum mass has been reduced by using further stellar orbital properties of 12 different stars orbiting Sgr. A*.

The estimated maximum masses are $6.5 \cdot 10^4$ M$_\odot$ with a semi-major axis of 150 AU for a circular orbit and $3.1 \cdot 10^4$ M$_\odot$ with a semi-major axis of 115 AU for a highly eccentric orbit. This maximum mass of the companion black hole corresponds to a intermediate black hole, which still is a type of black hole under investigation of its origin. The confirmation of a companion black hole will be a possibility in the coming decade of the 2030's with LISA, which can detect gravitational wave radiation that the black hole will - if existing.

Contents

1   Introduction

We have all gazed upon the sky on a clear night and wondered what is out there in the Universe. We have all observed the stars, the Moon and even planets from time to time. In the southern hemisphere it is even possible to see the Milky Way. But what is really out there beside stars, moons and planets?
Our Solar system is located in a galaxy called the Milky Way, but it is only one of billions of galaxies in the Universe. For many centuries our Galaxy has been an enthralling subject to study and in the past 100 years many groundbreaking discoveries have been made, especially in the study of what lurks in its nucleus.
Even though our own Galaxy's center is by far closest to observe, it is not without any problems. The interstellar medium blocks an amount of wavelengths and it is only possible to observe radio, infrared, x-ray and gamma-ray radiation.

Since the 1950's a powerful radio source has been detected from the galactic center[1]. In 1951 two Australian scientists, Piddington and Minnett, detected a clear radio wave signal (at 1210 and 3000 Mhz) in a small town close to Sidney. They used two small antennas, a 3 m diameter mobile dish and a large paraboloid located on top of Potts Hill. Due to lack of proper equipment they could only establish a raw limit to the objects size. Throughout the years and as technology and astronomical observation equipment evolved it has become possible to determine what lurks in the galactic center. In this decade as well, the region of the source was named Sagittarius A (Sgr. A) by the scientists Kraus, Ko and Matt and in 1960 it was confirmed that Sgr. A was located in the galactic center by Oort and Rougoor[1].

In February 1974 in Green Bank, Virgina, a strong radio emission was detected from the 1 parsec inner core of the galactic nucleus by the two scientists Balick and Brown[2]. The instruments had evolved significantly and they used a new interferometer consisting of three 26 m antennas, which could be up to 2.7 km apart from each other. 35 km from those, on top of a mountain, a fourth 14 m antenna was placed. They had good weather conditions and could detect a clear,

strong signal from the galactic center. The powerful and compact radio source was in a region of 1×3 arcsec and the angular diameter did not exceed 0.1 arcsec[1]. The radio source they detected was a supermassive black hole which in the 1980's was named Sagittarius A* (Sgr. A*)[2].

But the Milky Way is not the only galaxy with these characteristics. Similar observations have been made in other galaxies. Most galaxies have a compact region alike our Galaxy with dense gas and stellar population in its galactic nuclei. If the center emits a powerful electromagnetic emission in x-ray, radio and UV spectrum due to physical processes, it will be classified as an AGN - Active Galactic Nuclei.

There are different types of AGN's, but the most powerful are quasars. These objects are the most luminous and outshine their host galaxy. The activity originates from a supermassive black hole located in its center. This activity spikes if the black hole is active and consumes nearby matter rapidly in order to obtain high enough luminosity[3].

The Milky Way is not active in the same manner as a quasar. It is close to dormant, but spikes of activity happen once in a while and bright flares are observed from the hot gas in orbit around Sgr. A*[4].

Since the discovery of Sgr. A* a lot of progress in the study of black holes has been made, especially in the past few years.

In 2019 the first pictures of a black hole were taken with the Event Horizon Telescope. This black hole is located in the Messier 87 galaxy which is also located in the local Universe. It is not possible to get a direct image of a black hole since nothing can escape from it - not even light, ut the accretion disk surrounding the black hole lights up and this what was possible to observe[5].

In 2020 the Nobel Prize in Physics was given to Roger Penrose, Reinhard Genzel and Andrea Ghez for their work on black holes. The latter two received the Nobel Prize for their work on the black hole in the Galactic Center, namely Sagittarius A*[6].

Even though our knowledge concerning black holes has been broadened throughout the past decades, black holes are still a mysterious phenomenon. It is only possible to characterize three properties of a black hole - its mass, angular momentum and electric charge. A detailed explanation can be found in Section 2.3. When the mass of a black hole has been determined it opens a door to exploring further properties, e.g. its Schwarzchild radius.

In Åkesson & Kristensen (2019) the mass of Sgr. A* was determined using stellar orbits around the black hole. Through the orbital properties of these stars the mass could be determined using Kepler's 3. law. The results obtained from the orbital properties are used in further work throughout this thesis. The work in Åkesson & Kristensen (2019) is based on publications of Ghez et al. (2003 & 2005), Meyer et al. (2012), Boehle et al. (2016) and Abuter et al. (2018) using the stars S0-1, S0-2, S0-16, S0-19, S0-20, S0-38 and S0-102.
In order to compare the orbital data with more recent results, orbital properties from Peißker et al. (2020a) have been used. This publication have data on the stars S0-2, S0-19, S0-29, S0-38, S0-42, S0-60, S0-62 and S0-64.

It is possible for many supermassive black holes to be part of a binary system with another black hole. Naoz et al. (2020) present the possibility of Sgr. A* being in a binary system and this thesis will continue their work on determining and narrowing the mass interval of a potential companion black hole.

Binary black hole systems can be formed in several ways depending on their size. If the system consists of two supermassive black holes, it would be formed in a galaxy merger. If the system consists of two stellar mass black holes it can be formed either by common envelope or dynamical encounters. Further explanation on these formation possibilities can be found in Section 2.10.1.
Since it is not known if the Milky Way has collided with another galaxy hosting a supermassive black hole in the past, it would be very surprising if the companion black hole would be a supermassive black hole.
Thus the companion black hole must be either a stellar mass black hole or even

an intermediate mass black hole (IMBH). These IMBH are somewhat mysterious objects which no one actually knows how form. One theory states that they must be a result of two stellar mass black holes merging. [24]

In the pursuit of the expected mass of the companion black hole it is assumed that Sgr. A* and the companion black hole are part of a triple hierarchical system, in order to apply the Konzai-Lidov mechanism. This system consists of an inner orbit formed by Sgr. A* and the companion black hole and an outer, much wider orbit will be formed by a star. Naoz et al. (2020) use the star S0-2 and this thesis will test different stars in orbit of Sgr. A* in order to reduce the mass regime. This thesis will be using the Konzai-Lidov approximation in order to determine the mass interval and semi-major axis of the companion black hole. Thus the mass and type of black hole can be estimated.

In the future it will hopefully be possible to observe the galactic center with LISA when it launches in the 2030's. With LISA it can be confirmed if there is a companion black hole lurking in the center of the Milky Way with Sgr. A*.

2   Theory

In order to use the data and methods this thesis revolves around, it is important to have some background knowledge. This section includes a summary of the basics of black holes as well as their properties and formation. Furthermore, it will include a summary of black hole binary systems as the possibility of a companion black hole is investigated. There is a likelihood of the two black holes under consideration merging in the future, thus a summary of black hole mergers and gravitational waves is also included.

2.1   What is a Black Hole?

A black hole is a region in space where nothing - not even light - can escape due to the strong gravitational field. If an object enters the black hole it can only escape if its escape velocity is greater than the speed of light. Since the speed of light is the limiting propagation velocity of any physical object it is not possible for any object to escape a black hole[7].

2.2   Formation of Black Holes

After establishing the theory of a black hole residing in the center of the Milky Way it is of interest to explore how black holes are formed.
A theoretical model on how a black hole is formed is from a collapsar - a special type of supernova. These stellar objects are very massive and result from the collapse of stars more than 30 $M_\odot$ [7]. These objects are rotating very rapidly and are thought to have lost their outer layers of hydrogen and helium due to nuclear fusion in the different stages of its lifetime. The core of such stars is too massive to be a white dwarf or a neutron star thus the core will become a black hole when the thermonuclear reactions cease.

When a massive star is at the end of its lifetime it will become a supergiant. These stars are made of an onion-like interior where each layer contains different elements. When the core of an aging massive star progressively gets hotter as it

contracts, it will ignite different stages of nuclear fusion in the different layers. In the last stage of nuclear fusion the core will be converted into iron. This iron core is unable to undergo further fusion and can no longer create heat. The core will become unstable when the core mass exceeds the Chandrasekhar limit at 1.4 $M_\odot$ and the degenerate electron pressure can no longer hold the core stable [7]. This leads to a rapid core collapse which creates a shock wave ejecting material from the star, and thus an explosive supernova is created.

As a supernova undergoes core collapse it can result in two fates: becoming either a neutron star or a black hole. It depends on the mass of the initial star; if the star is more massive than $\sim$25 $M_\odot$ it will end its life as a black hole. Otherwise the remnants will form a neutron star. [8].

When a black hole is formed by a rapidly rotating progenitor star it will quickly form an accretion disk from the surrounding stellar material. The infalling material will form a rotating disk aided by the stars rotation. Some of the material will not fall into the black hole but will be ejected in jets along the rotation axis of the accretion disk. These jets are so powerful that they break through the star's surface within 5 to 10 seconds after being formed. Due to the short period of time it takes a black hole to accrete the inner core these bursts are very short lived. The accretion disk will no longer produce jets after the core is accreted [7]. It is possible to observe these intense gamma-ray bursts from Earth if the jets are aimed in the right direction [7].

2.2.1 Mass ranges of Black Holes

Black holes can exist in different mass ranges, Figure 1 shows the different observed ranges for compact objects such as white dwarfs, neutron stars and black holes. The masses in the chart are relative to the mass of the Sun.
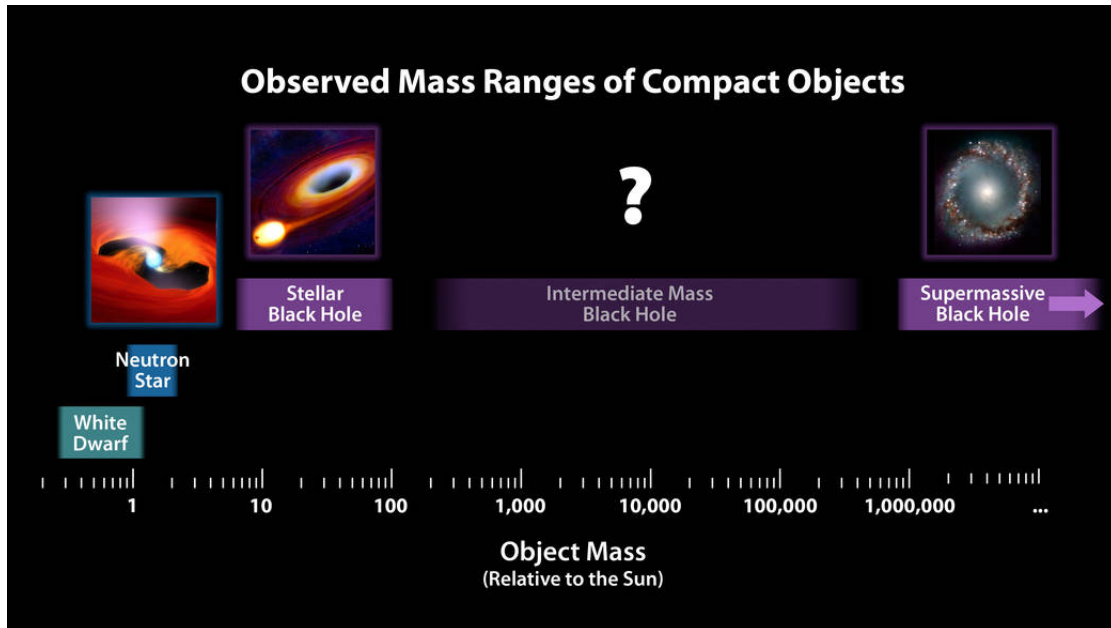
Figure 1: Mass chart of observed mass ranges of compact objects relative to the mass of the Sun. Figure from NASA website [9].

Supermassive black holes, such as the Sgr. A*, can have masses in range of 10^5-10^9 M$_\odot$ [8]. These black holes exist in the center of many galaxies and the formation of supermassive black holes has been theoretically speculated. One theory suggests that they are formed by collisions between galaxies. Another, that they are formed in extension to the formation process from Intermediate-mass black holes (IMBH).

The IMBHs have a mass range between $10^2 - 10^4$ M$_\odot$ [8]. The formation of these objects are still being investigated. In other galaxies several candidates have been found which are too big to be stellar-mass black holes, which have a mass range of 3-15 M$_\odot$ or so [8], and are too small to be classified as supermassive black holes [7][10]. In Section 2.11.2 further theories about IMBH are discussed. The correlation of IMBHs with the cores of globular clusters and low-mass galaxies suggests that they may have been formed in either core collapse of a supermassive star formed by mergers of stars or by mergers of stellar-mass black holes. The stellar-mass black holes are formed as a result of the collapse of a star.

In theory black holes could have been formed in the early stages of the Universe

creation. These are called primordial black holes and presumably have masses between 10^{-8}kg $- 10^5$M$_\odot$ [8].

2.3 Properties of Black Holes

When considering a black hole, only three properties are considered; mass, electric charge and angular momentum. The term "Black Holes have no hair" is often used, where the hair symbolize properties of the infalling matter. Since nothing can escape a black hole, all information about an infalling object will be lost when it enters the event horizon. All information possible to measure is determined through fields outside the black hole. [7]

2.3.1 Mass of a Black Hole

It is possible to determine the mass of a black hole by measuring the semi-major axis and period of a star orbiting the black hole. Using the Newtonian version of Kepler's third law, the combined mass of the black hole and the orbiting object can be found through [8]:

$$(M_1 + M_2) \propto \frac{a^3}{P^2}, \tag{2.3.1}$$

where M_1 and M_2 are the masses of the black hole and the orbiting object, respectively, a is the semi-major axis of a star in an elliptical orbit in AU and P is the period in years.

Since the mass of a black hole is usually much greater than the mass of the star, $M_1 \gg M_2$, the approximation $M_1 + M_2 \simeq M_1 = M$ [8] can be used:

$$M \propto \frac{a^3}{P^2}, \tag{2.3.2}$$

where M is the estimated mass of the black hole, including all the material it absorbs.

2.3.2 Electric Charge

The second property that can be measured is the total electric charge possessed by a black hole. This is a long range interaction which can be measured in the

vicinity of the hole. Just like gravity, it acts over long distances.

A black hole is not expected to possess any significant electric charge, if any. It is often neglected when investigating black holes. Due to the negatively charged electrons from the interstellar medium, any positive charge from the black hole would quickly be neutralized.

Even if the black hole in theory could possess some electric charge, it can not have any magnetic field of its own. If a magnetic field is detected it is associated to the accretion disk around the black hole. When a star collapses to form a black hole, the star can possess a magnetic field. This field must be radiated away before it can settle down inside the event horizon. The theory suggests that the star does this by emitting electromagnetic and gravitational waves [7].

2.3.3 Angular Momentum

The angular momentum is the third property of a black hole which is measurable. The angular momentum of an object is related to how the mass distribution over the volume of the object is and how fast its rotation is. The object in this case is a black hole. If a star collapses into a black hole, the rotation will speed up and the mass will be moved towards the center.

If the black hole is rotating, the upper limit will be [8]:

$$L_{\max} = \frac{GM^2}{c}, \tag{2.3.3}$$

where $L_{\max}$ is the maximum angular momentum, M is the mass of the black hole G is the gravitational constant and c is the speed of light in vacuum.

It is not possible to exceed this limit as this would result in no event horizon and a naked singularity would appear. The hypothesis of the Cosmic Censorship states that a naked singularity cannot exist since it will always be clothed by an event horizon. This hypothesis is not proven, but only a conjecture [11].

2.4 Schwarzchild Radius

When the mass of the black hole is determined, the Schwarzchild radius can be found. The Schwarzchild radius is the distance measured from the center of a

non-rotating heavy object to its event horizon. Inside the Schwarzchild radius nothing - not even light - can escape since its escape velocity must be greater than the speed of light. This is due to the gravity being too massive for any object to escape a black hole. An object is classified as a black hole if its radius is smaller than its Schwarzchild radius. The Schwarzchild radius is given by [12]:

$$R_S = \frac{2GM}{c^2}, \qquad (2.4.1)$$

where R_S is the Schwarzchild radius, G is the Gravitational constant, M is the mass of the black hole and c is the speed of light in vacuum.

If a black hole has the same mass as our Sun (1 $M_\odot$) its Schwarzchild radius will be ~ 3 km. The Suns radius is 696.000 km, which illustrates how small the Schwarzchild radius is and how dense a black hole actually is [7].
Sgr. A* has a mass of $\sim 4 \cdot 10^6$ $M_\odot$ and its Schwarzchild radius will be $\sim 10^7$ km which corresponds to ~ 0.08 AU.

2.5 Structure of a Rotating Black Hole

A non-rotating black hole has a simple structure which consists of a singularity and an event horizon. Since it does not rotate the event horizon will be a sphere with a radius equal to its Schwarzschild radius R_s [7].
The event horizon is a spherical boundary and a mathematical surface. What enters the event horizon will not escape again.

If a black hole is rotating its called a Kerr black hole after the New Zealand mathematician, Roy Kerr who worked out the structure in 1963 [11].
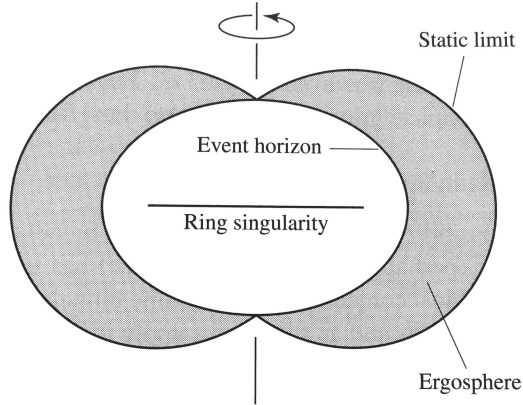
Figure 2: The structure of a Kerr black hole which has maximum rotation. The ring singularity is seen edge-on. The event horizon is located at the equation with a radius of: $r = \frac{1}{2}R_S$. Figure is Figure 17.22 from Carroll, B. W. & Ostlie, D. A. (2017), *An Introduction to Modern Astrophysics* [8].

Figure 2 shows the structure of a black hole with maximum rotation. Instead of being a point, the singularity has been distorted into a flat ring. Due to the rotation, the event horizon is now shaped as an ellipsoid. The phenomenon frame dragging will appear when a massive object spins and thus will induce a rotation in the surrounding spacetime. When a massive object spins the rotating spacetime will produce a local deviation from the non-rotating frame that describes the Universe at large [8].

The frame dragging near a Kerr black hole is so severe that a non-spherical region outside the event horizon will appear. This region is called the ergosphere and in this region any particles must move in the same direction as the rotation of the black hole. Within the ergosphere the particles can not remain in the same angular coordinate, due to the spacetime rotating so rapidly that the particle must travel faster than light to remain in the same angular coordinate.
The static limit is the outer boundary of the ergosphere. Beyond the boundary the frame dragging effect diminishes and the particle can remain in the same coordinate [8].

2.6 Lifespan of a Black hole

2.6.1 Active or dormant?

Most of bright galaxies have a supermassive black hole in the central region. This is revealed by the spectra of gas and stars in this region. Even though a bright galaxy contains a supermassive black hole it is not necessarily an active galaxy. The black hole must be accreting gas rapidly to have a high enough luminosity to outshine the stars in the host galaxy [13].

As long as there are stars and gas to be absorbed in the vicinity of the black hole, it will remain active. At some point all the matter will have been absorbed and the black hole will become dormant.

If the stars are in a safe distance of being absorbed by the black hole they can maintain a stable orbit for a long time until the energy of the stars or gas will be removed due to the tidal forces from the black hole and the friction in the gas affecting the star. If all the energy is lost, the stars or gas cloud will orbit closer and closer to the black hole. At the end they will be absorbed by the black hole and the hole will have a spike in activity [14]. These spikes in activity can also be seen in Sgr. A*. The Milky Way is not an active galaxy and is close to dormant but when monitoring the orbit of the S0-2 star near Sgr. A* some activity was observed. The observations when monitoring S0-2, showed bright flares originating from the hot gas orbiting close to Sgr. A* [4].

2.6.2 Hawking Radiation

In theory a dormant black hole can evaporate if the Universe will keep expanding and all stars die. This is due to Hawking radiation [8].

The evaporating process is due to pair production, which will lead to the formation of a particle-antiparticle pair just outside the event horizon of the black hole. The particles will mostly recombine and disappear, but it is possible for one of the particles to enter the event horizon while the other escapes. The gravitational energy of the black hole was used to create the particle pair and since energy is equal to mass then the particle which escapes will carry away a portion of the

black hole's mass. The process can be found in Figure 3.
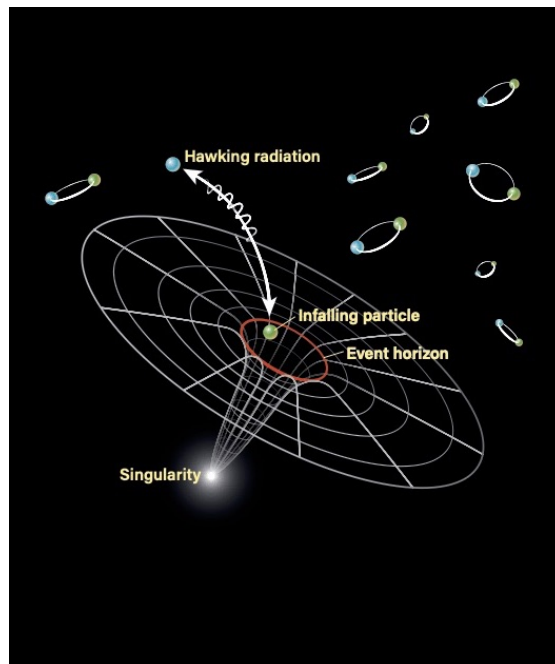
Figure 3: Process of Hawking Radiation. Figure from Astronomy.com [15].

This will over time reduce the black hole's mass and at last it will evaporate. This process is very slow and the time it will take for a primordial black hole to evaporate is:

$$t_{\text{evap}} = 2 \cdot 10^{67} \left(\frac{M}{M_\odot} \right)^3 \text{yr.} \tag{2.6.1}$$

This means that a primordial black hole with a mass at $1.7 \cdot 10^{11}$kg would evaporate in 13 billion years. Since the Universe is 13.7 billion years old, a primordial black hole with this specific mass could be in its final stage of evaporating now and be detected. In the final stage the evaporation will proceed rapidly and will result in a burst of elementary particles. An empty region of flat spacetime could possibly be the result of such an explosion.

The final burst of the Hawking radiation will result in high energy gamma rays (≈ 100MeV) released at a rate of 10^{13} W. The gamma rays will be released together with electrons, positrons and other particles. It would be possible to observe the

13

additional gamma rays' origin from the subsequent decay of these particles with satellites orbiting the Earth. By measuring the cosmic gamma-ray background at this energy it is theoretically be possible to detect Hawking radiation, but to this date nothing yet has been detected corresponding to a deceased primordial black hole. The non-existing results implies that within every cubic light-year of space there cannot be more than 200 primordial black holes with the mass $\sim 10^{11}$ kg [8].

2.6.3 Accretion rate

There is a limit for the maximum possible luminosity for an accreting black hole called the Eddington limit or the Eddington luminosity [13]. If the luminosity is too high then the gas surrounding the black hole will be blown away due to radiation pressure. The luminosity when the outward radiation force is equal the inward gravitational force is:

$$\frac{\sigma_e\, L_e}{4\pi\, c\, r^2} = \frac{GMm_p}{r^2}, \tag{2.6.2}$$

where L_e is the Eddington luminosity, σ_e is the Thomson cross section with $\sigma_e = 6.65 \cdot 10^{-29} \mathrm{m}^2$, m_p is the proton mass, M is the mass of the black hole and r is the distance from the black hole.

Since the ratio of radiation force to gravitational force is independent of distance r from the black hole, then the Eddington luminosity is:

$$L_E = \frac{4\pi\, G\, m_p\, c}{\sigma_e}\, M. \tag{2.6.3}$$

The ionized gas will be accelerated outwards if the luminosity is greater than the Eddington limit and thereby the accretion will cease. The maximum accretion rate a black hole can have will be:

$$\dot{M}_e = \frac{L_e}{\eta\, c^2} = 2\, \mathrm{M}_\odot\, \mathrm{yr}^{-1} \left(\frac{M}{10^8\, \mathrm{M}_\odot} \right) \left(\frac{\eta}{0.1} \right)^{-1}, \tag{2.6.4}$$

where η is a dimensionless number, often referred to as the efficiency of the black hole. For a typical active galactic nucleus $\eta \approx 0.1$ [13].

In equation 2.6.4 a simple spherical accretion model is described for the maximum possible accretion rate $\dot{M}_e$. It is possible to exceed this limit when models

which are not spherically symmetric are considered. If the mass accretion primarily occurs along the equator of the disk but the radiation emerges along the disk axis it is possible to exceed this limit [16].

2.7 Tidal forces

When an object, e.g. a star, orbits a black hole it will be torn apart by tidal forces if it orbits within a certain distance to the black hole. The tidal forces are differences in the gravitational pull at different points in an object.

These forces are the explanation of the ocean tides and why the Moon always faces the same side towards the Earth. Tidal forces are also an explanation of why Saturn has rings [7]. In Figure 4 the different forces affecting the Earth can be seen. The centrifugal forces are marked with yellow arrows and the gravitational force from the Moon is marked with blue arrows. The parts of the Earth which are closer to the Moon will experience a greater pull than the opposite site. Which can be seen as the blue arrows differ in size.

If we look at the Earth from the perspective of the Moon, then it will be a three-dimensional object with a "top" and "bottom". These areas will be pulled inward and toward the center of the Earth, relative to the areas in the middle [17].

It is important to estimate how close an object really can be to a black hole before it will get torn apart by the tidal forces. An explanation can be found in the following section.
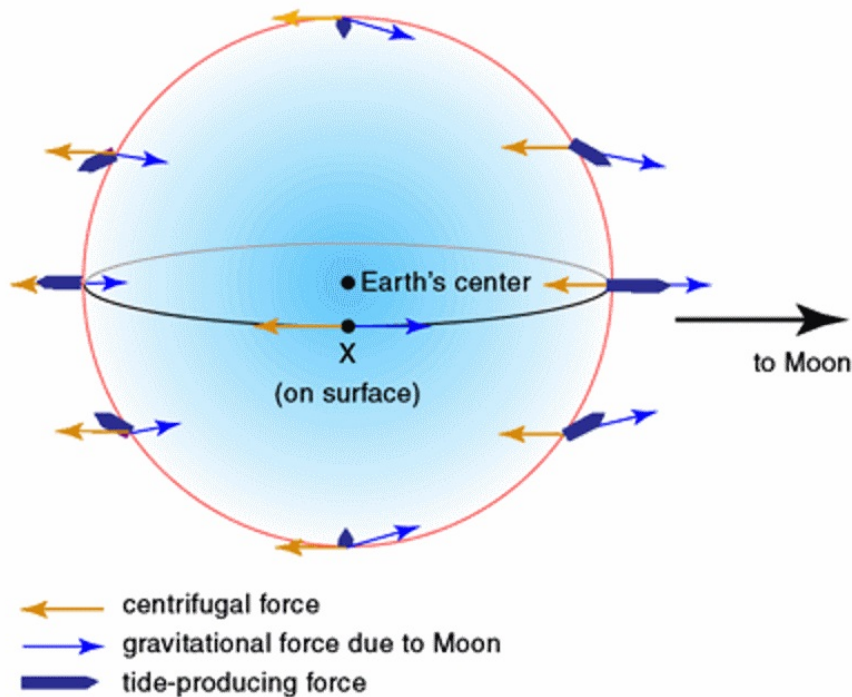
Figure 4: Schematic of the Earth and the pull of centrifugal forces, gravitational forces and tidal forces. Illustration from Forbes website. [17]

2.7.1 Roche Limit

If considering a collection of small particles near a massive object, e.g. a black hole, the particles will tend to be pulled close to each other due to the gravitational attraction between them. Since the particles differ in distance from the massive object they also differ in gravitational pull, and the tidal forces from this object will keep them separated.

When the particles are at a certain distance from the object, the tidal forces will be as strong as the gravitational force between the particles. When exceeding this limit, the particles will be torn apart. The distance where this occurs is called the Roche limit r_R defined as [13]:

$$r_R = \left(\frac{2\,M}{m}\right)^{1/3} r, \tag{2.7.1}$$

16

where M is the mass of the massive object, m is the mass and r is the radius of the less massive object.

Inside the Roche limit, smaller objects will be torn apart due to the tidal force exceeding the gravitational force. A star or any other object will be torn apart if it enters the Roche limit of a black hole.

If S0-2 or any other star in the vicinity of Sgr. A* will orbit too close to the black hole it can enter Sgr. A*'s Roche limit and thus be torn apart. By comparing the periapse distance of the star to the Roche limit of the black hole it is possible to determine if it will be in danger.

The periapse can be found using the semi-major axis and eccentricity of the stars orbit [8]:

$$r_p = a \left(1 - e \right). \tag{2.7.2}$$

In Åkesson & Kristensen (2019) the Roche limit of Sgr. A* is determined to be in the range of 1.31-2.26 AU and the periapse distance of S0-2 is 92 ± 4 AU. Thus S0-2 is not in any danger of being torn apart by Sgr. A* [18].

When the mass interval of the companion black hole is found it is possible to determine whether or not S0-2 or any other stars in the vicinity of the companion black hole are in danger.

2.8 Mass Transfer

There are different ways that mass can be transferred from a massive star to a black hole. One is through mass transfer by filling its Roche lobe. Another is mass transfer through stellar winds.

2.8.1 Roche Lobe

If a star orbits too close to a more massive object, e.g. a black hole or a larger star, it can transfer its mass.

In Figure 5 the Roche lobe of a binary star system is shown. The system could also be a black hole and a star, which is assumed in this case. On the figure the

smaller star, a black hole in this case, and the (larger) star will be surrounded by two surfaces, marked with dashed lines, called Roche lobes. These surfaces are not physical surfaces, but a mathematical construction.

The material will be gravitationally bound to the object inside this lobe. When the star gets older and swell up it will fill its Roche lobe. When the material leaks over its Roche lobe it will no longer be gravitationally bound to the star and will either fall into the black hole or escape the system.

The two Roche lobes touch at a point called the inner Lagrangian point, which can be considered a balance point between the two objects. At this point the gravitational and rotational effects cancel each other out and any mass transfer occurs through this point.

In a case where the objects in the binaries are far apart, during the stars red giant stage, the Roche lobe will not be filled up by the stars surface and only a small amount of mass will be transferred. This is called a detached binary and the star will continue its life as if it was isolated[7]. It is illustrated on the left hand side of Figure 5.

When the two objects are close enough, as the star reaches its red giant stage, it will fill up or overflow its Roche lobe and can transfer its mass to the black hole. This is called semidetached binary and is illustrated on the right hand side of Figure 5 [7].
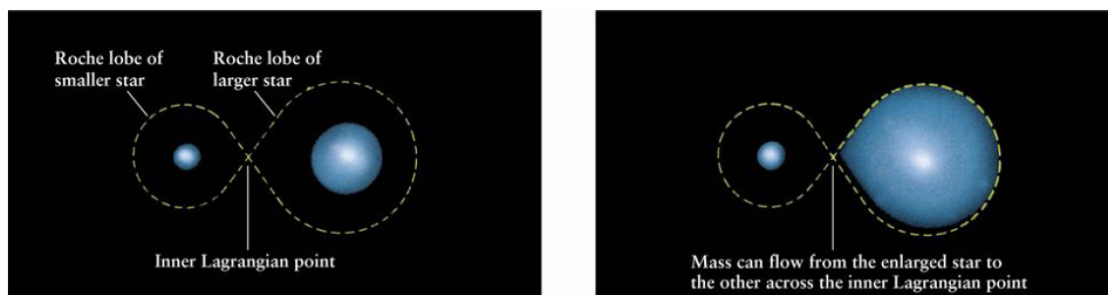

Figure 5: A close binary star system. *Left*: A detached binary. *Right*: A semidetached binary. Figure 19-21 from Freedman, R.F, Geller, R. M & Kaufmann III, W.J. (2014). *Universe* [7]

2.8.2   Stellar Winds

The outflows of gas from a star's atmosphere are called stellar winds. The temperature of the star affects what these stellar winds contain. In cold stars, e.g. red giants, they are induced mainly by radiation pressure on dust which is formed in the outer, colder layers. In massive hot stars, e.g. O and B main sequence stars, the stellar winds are powered by radiation pressure from photons [19].

It is possible for a companion to capture and absorb some of the ejected mass. The amount of captured mass will depend on how much is lost and the relative velocity of the wind with respect to the companion [19].

2.9   Observing Black Holes

It is not possible to observe a black hole directly since it does not emit any radiation or light, but it *is* possible to observe the accretion disk surrounding the black hole. This phenomenon was pictured in 2019 at the Messier 87 galaxy using the Event Horizon Telescope. The picture found in Figure 6 is the first image of a black hole ever taken. It is not possible to observe the black hole directly, but only its shadow. The event horizon is around 2.5 times smaller than the shadow the black hole cast. It measures $\sim 40 \cdot 10^9$ km across. It is about 40 μparcsec across. For size comparison it is equivalent to measuring the length of a credit card on the Moon's surface [5].

Figure 6: Picture of the black hole in Messier 87. Picture from ESO website [5].

2.9.1 Active Galactic Nuclei

A compact region with dense gas and star populations can be found in most galaxies and is called galactic nuclei. Approximately 1% of these galaxies will have an active galactic nuclei (AGN). These AGN's physical processes will generate powerful electromagnetic radiation in the X-ray, radio and ultraviolet spectrum. The most powerful sources of the radiation originate from quasars. These quasars are so luminous that they outshine their host galaxy. The activity in quasars originate from central black holes. It is believed that most of the galaxies with an active nuclei contain a supermassive black hole [3].

While ordinary stars emit in the ultraviolet, visible and infrared wavelength, luminous objects such as quasars emit in radio, optical, x-ray and gamma-ray wavelengths.

The electromagnetic radiation is emitted from different regions of the accretion disk surrounding the black hole. If the emission comes from the part of the accretion disk which is closest to the black hole then the effective temperature of the radiation will be higher.

Besides observing the accretion disk surrounding the black hole, it is also possible to observe relativistic jets, which are described in Section 2.2.

2.10 Black Hole Binary Systems

A binary black hole system consists of two black holes in a close orbit around each other. As for singular black holes, the binary black holes system can be divided into types of black holes depending on how they are formed. It is often stellar-mass black holes or supermassive black holes. The formation of these will be explained in the following sections.

2.10.1 Formation of Stellar Mass Binary Black holes

Stellar mass black holes are formed by massive stars' final stage of evolution: when they explode as a supernova. As an alternative the black holes can be formed as a binary by dynamical encounters in a dense star cluster [20].

The first scenario of formation of stellar mass binary black holes are formation through common envelope isolated, meaning that the system is not affected by any other objects, in the left hand side of Figure 7 this scenario is illustrated.
In the first stage two massive stars on the main sequence (MS) are gravitationally bound. At some point the most massive star (primary) will leave the MS when its core has finished the hydrogen burning. Then the radius of the star will inflate and it will grow significantly. It will enter the next stage and become a giant star with a Helium core and Hydrogen envelope. If the giant star's radius has grown enough to fill its Roche lobe, then mass transfer will occur, as described in Section 2.8.1.
After going through further evolutionary stages the giant star will collapse to a black hole.
In the fourth stage the secondary star will leave the MS and undergo the same evolution as the primary. It is then possible for the two stars (or now a black hole and a star) to enter a common envelope stage.
If the two cores enter a common envelope, their envelopes will stop co-rotating

21

with their cores.

Since the stellar core and the compact remnant are in the same envelope which is not rotating, they will start spiralling in due to the gas drag from the envelope. The envelope can become more loosely bound by heating. Part of the core's orbital energy will be lost due to the drag and can be converted into heating of the envelope.

If the envelope is bound loosely enough, the envelope can be ejected and the binary will survive as a compact remnant and a naked stellar core.

Due to the spiralling in the common envelope stage, the orbital separation of the two objects will be very small and less than the initial separation.

If the stellar core evolves into a black hole and therefore a binary black hole system will be formed, then the semi-major axis will be very short. Over time the black holes will merge.

In the case where the common envelope is not ejected, the two objects will keep spiralling in till they merge and become a single black hole and a binary black hole system is not possible. [19]

The second scenario is formation of binary black holes in star clusters. This formation is illustrated on the right hand side of Figure 7.

In the first stage we will again start with two main sequence stars, where the primary will undergo its evolution to a giant star with a Helium core and then to a black hole.

If the binary system interacts with a single object and this object replaces one of the objects of the binary, then a dynamical exchange is occurring. It is known that massive objects can acquire companions through dynamical exchanges - especially massive objects as black holes are efficiently forming new binaries through these exchanges [20].

When such a three-body encounter is occurring, the third body will absorb a fraction of the internal energy from the binary star. If this binary is tightly bound, these encounters will harden the binary star (or object). Meaning that the binding energy will increase by reducing its semi-major axis. This is called dynamical hardening. If the binary system consists of two black holes, this hardening can
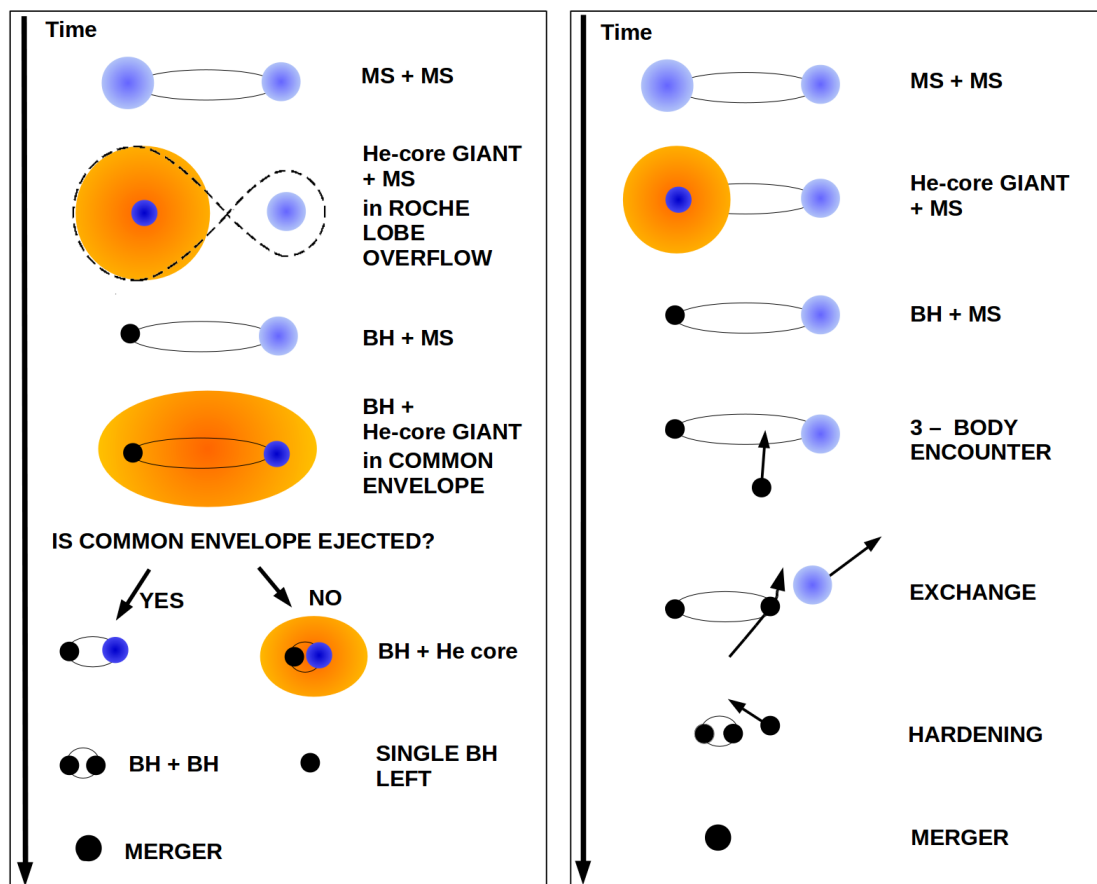
speed up the merger [20].

Figure 7: *Left:* Isolated formation through common envelope of BBH. *Right:* Dynamical formation of BBH in star clusters. Figure 2 from Mapelli (2020) [20].

2.10.2 Formation of Supermassive Binary Black Holes

When two massive galaxies merge while both hosting supermassive black holes it will create a binary system of super massive black holes. As a result of the merger the two black holes will migrate towards the center of the combined system as a result of dynamical friction. The black holes can then enter a binary system though it depends on the trajectory of the galaxies [8].

In the center of the merged galaxy the two black holes orbit each other, which affect the surrounding stars. A dynamical exchange can happen as described in the former section. If the total mass of the stars ejected from the central region is

equivalent with the mass of the black holes, then it is possible for enough angular momentum and energy to be carried away by the stars. Then the two black holes will spiral in towards each other and, eventually, the two black holes will merge and create an even larger supermassive black hole [8].

2.11   Result of Merging Black Holes

The former section contains a description of how the binary black hole systems are formed and their fate of merging. When the black holes eventually merge, they will release gravitational waves, which are possible to detect.

In Figure 8 an illustration of the different stages in a merger can be found. The six different stages are:

1. Two supermassive black holes are located in the core of massive galaxies.

2. The galaxies merge and their black holes will spiral towards each other and eventually merge and become one.

3. In the merger of two supermassive black holes gravitational waves and light - x-rays in particular - will be released.

4. The merging black holes will accrete the surrounding hot gas, which emits x-rays.

5. Some of the x-ray emission is expected to be at a frequency corresponding to the gravitational waves originating from the black hole merger.

6. A corona of hot, x-ray emitting gas will form and jets of particles can be launched with speeds close to the speed of light.
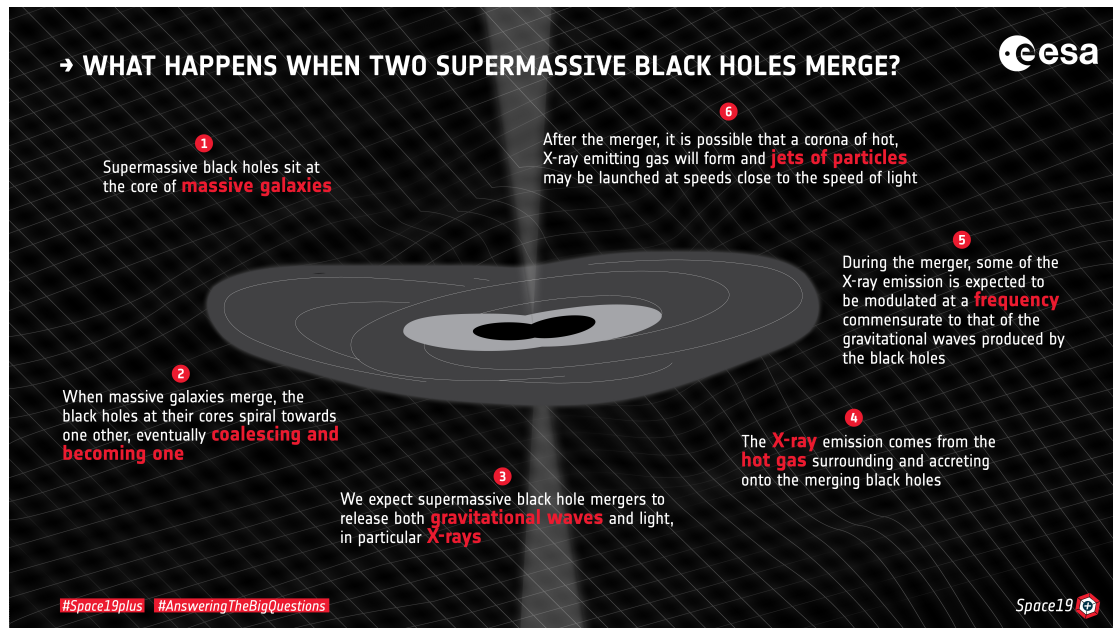
Figure 8: Illustration of the process of merging two supermassive black holes. Illustration from ESA website [21].

2.11.1 What Are Gravitational Waves and How Can We Detect Them?

When massive objects such as black holes or neutron stars collide it will disturb the space-time. When two massive objects orbit each other they will disrupt the space-time in such a manner that "waves" will curve the space-time and propagate in all directions away from the source, similar to a rock thrown in a still lake. Then the waves will propagate away from the point of impact.

These cosmic waves travel with the speed of light and they carry information with them about their origin. The strongest gravitational waves (GW) originate from the collision of black holes or neutron stars but it is also possible to detect gravitational waves from supernovae and the rotation of non-spherical neutron stars [22].

It is possible to detect gravitational waves throught the LIGO experiment (Laser Interferometer Gravitational-wave Observatory). LIGO is a gravitational wave observatory consisting of two large interferometers located 3000 km apart in the USA [22].

In collaboration with the European gravitational wave observatory Virgo, they de-

tected the first gravitational waves of two black holes merging in September 2015 and have later detected several other events [22].

Further reading about LIGO, its specifications and details on their work can be found on their website. [1]

2.11.2 Formation of Intermediate-mass Black Holes

One of the biggest questions in the theory of black hole formation is how intermediate-mass black holes are formed. In the former sections the formation of stellar mass and supermassive black holes are described, but the formation of intermediate black holes are still a mystery.

Throughout the years evidence of black holes in the low and high end of the chart have been confirmed and found. But the black holes in between these are not as common.

In 2003 proof of an intermediate black hole was found. It was estimated to be around 5000 $M_\odot$ ± 1000 $M_\odot$ which put it in the category of IMBHs. Again in 2009 another candidate to an IMBH was found and estimated it to have a minimum mass of 500 $M_\odot$. [23]

These observations show that there is something in between stellar mass and supermassive black holes.

The theory of IMBH being formed by two stellar mass black holes was confirmed in 2019 when detecting the gravitational wave signal GW190521 [24]. The signal was consistent with the merger of two stellar mass black holes of masses $\approx 85 M_\odot$ and $\approx 66 M_\odot$. The calculated mass of the remnant was $\approx 142 M_\odot$, which is consistent with an IMBH [24].

In 2019 LIGO had detected ten binary black hole merger events, all of them in the range of stellar mass black holes. [25]. In Figure 9 the different observed mergers can be found in the different mass ranges. The event GW190521 is not included in the chart.

---

[1] https://www.ligo.caltech.edu/

Further theorizing about the formation of IMBHs is that they originate from populations III stars (very massive stars) and from wandering black holes. These theories are described in the review by Greene et al. (2020) [26].
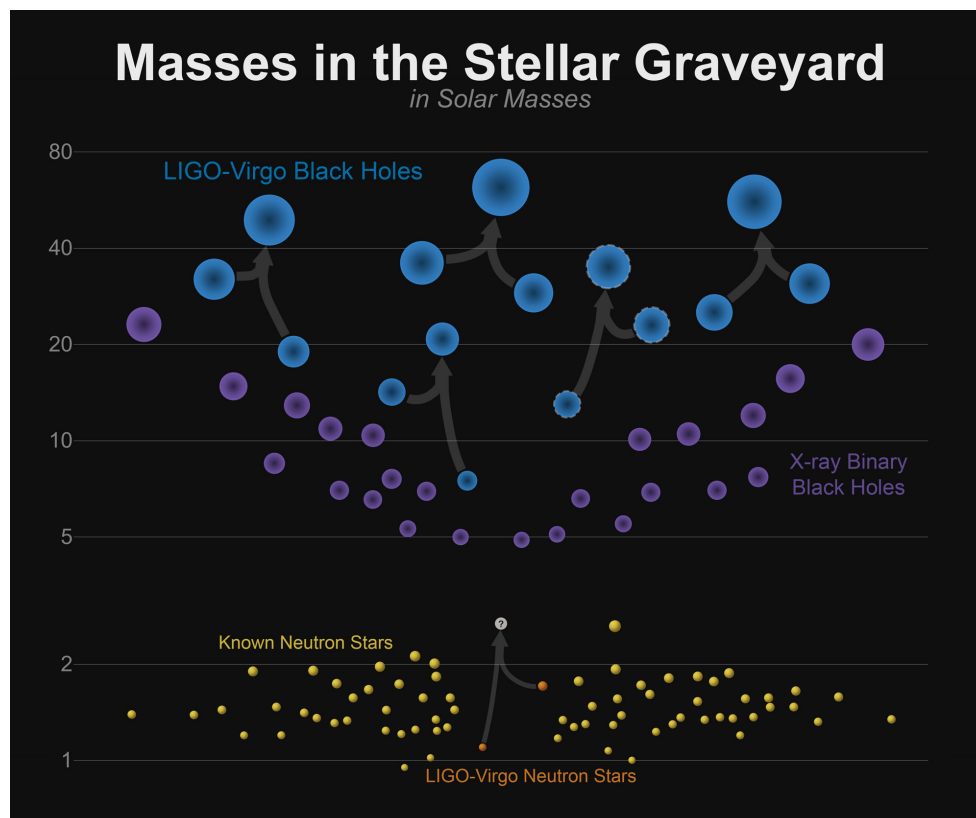

Figure 9: The illustration show the mass chart of different objects. The arrows show mergers of BH/NS. *Blue:* Black holes measured by GW observations. *Purple:* Black holes detected by electromagnetic observations. *Yellow:* Neutron stars detected by EM observations. *Orange:* Neutron star merger in event GW170817. Remnants are yet to be classified. Illustration from LIGO website [27].

In this theory section the basics about black holes have been explained. An explanation about tidal forces and mass transfer has been given. Followed by how black holes are being observed and how binary black hole systems are formed.
At last a summary of black hole mergers have been given, including a short summary of gravitational waves and the mysterious intermediate black holes.
This leads to the next section about the Konzai-Lidov mechanism and three body problems.

3 Methods

In this section the Konzai-Lidov approximation [29] will be explained and put to use. This approximation is used since this thesis considers a triple body system with Sgr. A*, a companion black hole and a star.

In this section a short summary of the Konzai-Lidov mechanism is presented and then continued to the derivation of the equations used in Naoz et al. (2020) [28] in order to further work on their theory. The same approximations and assumptions made in Naoz et al. (2020) will also be utilized in this work.

3.1 Konzai-Lidov Mechanism

In the Universe it is very common to encounter triple systems. These triple systems can be almost impossible to solve but the two scientist Konzai and Lidov found a solution in 1962 and 1961 respectively [29].

They introduced a study of hierarchical systems with an inner binary being perturbed by an object on the outer, much wider, orbit.

Figure 10: A hierarchical three-body system consisting of the inner binary and outer orbit. The inner orbit consists of Sgr. A* and companion black hole and the outer orbit consists of the star S0-2. Figure 1 from Naoz et al. (2020) [28].

In the case studied here, the inner orbit is formed by Sgr. A* and the companion black hole, while the outer orbit is formed by a star (e.g. the star S0-2), which can be seen in Figure 10.

The stability of these hierarchical tripe systems require that the inner binary has a nearly Keplerian orbit and an outer binary in which the third body orbits the center of mass of the inner binary. The semi-major axis of the outer orbit must
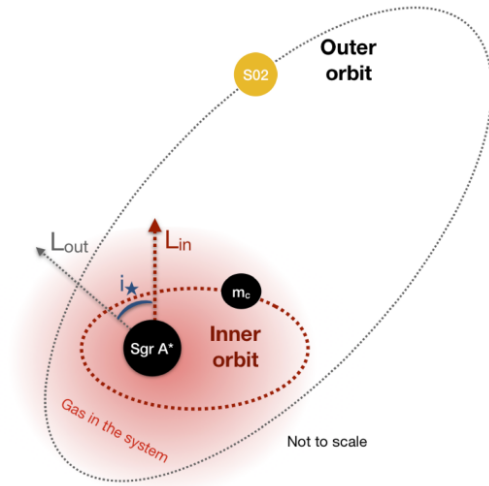
be much larger than the inner orbit. The perturber (i.e. the third body) must not make a close approach to the inner binary orbit. The Konzai-Lidov mechanism describes the stability regime in which a highly inclined perturber can produce large-amplitude oscillations in the eccentricity and inclination of the system [30].

3.1.1 The Hierarchical Three Body Secular Approximation

In order to simplify the three body system, the secular approximation can be considered. By assuming an inner binary consisting of a primary and secondary object, which are orbited by an object far away (e.g. a star in this case), then the secular approximation can be used. In this setting it is assumed the energy is conserved for each orbit separately and therefore the energy for the whole system is conserved. This approximation assumes that the semi-major axis of both orbits are constant and thus the dynamical behavior of the system is due to the exchange of angular momentum between the two orbits.
When using the secular approximation it is under the assumption that the line-density is inversely proportional to the orbital velocity and the orbits torque each other and only exchange angular momentum and not energy. It is possible for the orbits to change orientation and shape on timescales much greater than their orbital periods. The shape of the orbits can be changed due to oscillations in the eccentricity and inclination of the orbit. Their orbits semi-major axis will not change, but only the orbits placement compared to the reference plane and their semi-minor axis [30].

In this case the outer body is treated as a massless test particle. This yields a test particle approximation to the quadrupole level [29]. This is valid for ax-isymmetric outer orbit potential.

The outer body has no effect on the inner binary but will be perturbed by the inner binary's gravitational field. This is called the inverse Eccentric Konzai-Lidov (iEKL) perturbations [28].

If systems beyond the test particle approximation is considered then the next level

of approximation, called the octupole-approximation should be applied[31]. In the conventional hierarchical triple system the outer body perturbes the inner binary creating Eccentric Konzai-Lidov (EKL) oscillations. The EKL is a process where the inner orbit's inclination can flip its orientation from prograde to retrograde with respect to the total angular momentum. This can occur when considering the octupole level of approximation, where the inner orbit's eccentricity can reach extremely high values which can cause chaotic behavior. [29]

Further reading of the octupole-level of approximation and EKL can be found in the review of Eccentric Konzai-Lidov effect by Smadar Naoz (2016) [29].

3.2 Deriving the Equations

In order to use the equations and understand the theory, it is important to understand their origin. In this section the equations from Naoz et al. (2017) [31] are utilized in order to derive the equations used in Naoz et al. (2020) [28]. Zero spin for both black holes is assumed for simplicity. It is also assumed that the ratio of the semi-major axis of the inner and outer orbit is small, thus the outer orbit period is much longer than the inner orbital period. Since the star is treated as a massless particle $(m_\star \to 0)$ it is also assumed that its mass is negligible. This is also the case in both Naoz et al. (2017) and Naoz et al. (2020). In Naoz et al. (2017) they consider an eccentric planet (m_2) and a massless test particle (m_3) both orbiting a star (m_1), while in Naoz et al. (2020) they consider a companion black hole (m_c) and the star S0-2 $(m_\star)$ both orbiting Sgr. A* $(m_\bullet)$.

The aim of this work is to find an upper limit and therefore narrowing down the allowed regime where the mass of the companion black hole can exist in. To arrive to equation 13 in Naoz et al. (2020), which is applied in the results found in Section 6, it is needed to start with the equations they originate from. Thus first, the equations 1-3 and 5-6 from Naoz et al. (2020) will be derived.

First, equation 2 is derived from Naoz et al. (2020), using equation 15 from

Naoz et al. (2017):

$$\left.\frac{d\theta}{dt}\right|_{\text{quad}} = -\frac{15}{8}\,\eta\,\frac{2\pi}{P_2}\alpha^2 e_1^2 \frac{1-\theta^2}{(1-e_2^2)^2}\sin 2\Omega_2. \tag{3.2.1}$$

Here $e_1 = e_c$ and $e_2 = e_\star$. ω_c is pericenter angle. The pericenter angle describes the orientation of the plane compared to the reference plane and is measured from the ascending node of the orbital plane to the periapsis. It is defined by $\omega_c \equiv \varpi_\star - \Omega_\star - \pi$ in Naoz et al. (2020). In Naoz et al. (2017) it is assumed that $\varpi_\star = 0$ and this work adopts the same assumption in order to solve the equations. Ω_c is not well-defined because the reference plane is aligned with the inner orbit thus the companion black hole must have $\omega_c + \Omega_c = \text{constant}$ and it is chosen to set the constant to zero. Thus $\Omega_c + \Omega_\star = \pi \Rightarrow \omega_c = -\pi - \Omega_\star$.

This then leads to equation 2 in Naoz et al. (2020):

$$\frac{d\theta}{d\tau} = -\frac{15\,\pi}{4}\eta\,\alpha^2\,e_c^2 \frac{1-\theta^2}{(1-e_\star^2)^2}\sin 2\omega_c. \tag{3.2.2}$$

In both equation 3.2.2 and 3.2.1 $\eta = m_\bullet\,m_c/(m_\bullet + m_c)^2$ and $\alpha = a_c/a_\star$. The two equations differ by being denoted either with a 2 or $\star$. This is due to Naoz et al. (2017) having denoted the two objects 1 and 2, while in Naoz et al. (2020) the objects are denoted $\star$ for the star, $\bullet$ for Sgr. A* and c for the companion black hole. In both equations θ is dependent on the inclination i with $\theta = \cos(i)$, Ω_X is the angle of the ascending node relative to the X-axis, and e_X is the eccentricity. Equation 3.2.2 is the equation of motion for the inclination.

By setting $\dot{\theta} = 0$ it is possible to find the maximum and minimum inclination thus the values of the longitude of ascending nodes which satisfy the condition $\Omega_2 = \frac{n\pi}{2}$, where $n = 0, 1, 2....$ Ω_2 has a liberating and circulating trajectory. In the liberating region the trajectories are bound between two values of Ω_2. In the circulating region the trajectories represent the angles not constrained between two specific values. The time evolution of Ω for the quadrupole-level of approximation are defined by Equation 1 in Naoz et al. (2020):

$$\frac{d\Omega_\star}{d\tau} = -\frac{3\,\pi}{4}\,\eta\,\alpha^2 \frac{\theta\,Q}{(1-e_\star^2)^2}. \tag{3.2.3}$$

31

Arriving to equation 1 equation 16 in Naoz et al. (2017) is used:

$$\frac{d\Omega_2}{dt}\bigg|_{\text{quad}} = -\eta\,\frac{2\,\pi}{P_2}\,\alpha^2\frac{3\,\theta\,Q}{8\,(1-e_2^2)^2} \tag{3.2.4}$$

In both equations above $Q = 2 + 3\,e_c^2 - 5\,e_c^2\cos 2\omega_c$. The notation is the same as in equation 3.2.2.

I want to arrive to Equation 3 from Naoz et al. (2020):

$$\frac{d\varpi_\star}{d\tau} = \frac{3\,\pi}{8}\,\eta\,\alpha^2\frac{4 + 6\,e_c^2 - 3\,(1-\theta^2)\,Q}{(1-e_\star^2)^2}, \tag{3.2.5}$$

where $\varpi_\star \equiv \Omega_\star + \omega_\star$ is a sum of the angles. Depending on which object being considered it vary from being denoted with a $\star$ for the star to c for the companion black hole.

The variable $\varpi_\star$ is defined by the relation given in Naoz et al. (2020):

$$\frac{d\varpi_\star}{dt} \equiv \frac{d\omega_\star}{dt} + \cos i_\star\frac{d\Omega_\star}{dt}. \tag{3.2.6}$$

Furthermore it is used that $\theta = cosi_\star$. $i_\star$ is the angle of inclination of the plane relative to the reference plane.

To derive equation 3.2.5 I use the equations of motion which can be expressed as the partial derivative of the energy function $f(e_2, \omega_2, \theta, \Omega_2)$ from Naoz et al. (2017):

$$\frac{dJ_2}{d\tau} = \frac{\partial f}{\partial\omega_2} \tag{3.2.7}$$

$$\frac{dJ_{2,z}}{d\tau} = \frac{\partial f}{\partial\Omega_2} \tag{3.2.8}$$

$$\frac{d\omega_2}{d\tau} = \frac{\partial f}{\partial e_2}\frac{J_2}{e_2} + \frac{\partial f}{\partial\theta}\frac{\theta}{J_2} \tag{3.2.9}$$

$$\frac{d\Omega_2}{d\tau} = -\frac{\partial f}{\partial\theta}\frac{1}{J_2}. \tag{3.2.10}$$

From equation 3.2.6 it is clear that the equations 3.2.9 and 3.2.10 need to be used. Furthermore I use the canonical specific momenta (angular momentum) which is defined as equation 2 in Naoz et al. (2017):

$$J_2 = \sqrt{1 - e_2^2}. \tag{3.2.11}$$

In the equations of motion the Hamiltonian is present as $f = f_{\text{quad}} + \delta \tilde{f}_{\text{oct}}$ from equation 10 in Naoz et al. (2017). Since I only consider the quadrupole-level due to $m_\star \to 0$, then $f = f_{\text{quad}}$:

$$f_{\text{quad}} = \frac{(2 + 3\,e_1^2)\,(3\,\theta^2 - 1) + 15\,e_1^2\,(1 - \theta^2)\,\cos(2\,\Omega_2)}{(1 - e_2^2)^{3/2}}, \tag{3.2.12}$$

which is defined by equation 6 in Naoz et al. (2017).

In equations 3.2.3, 3.2.2 and 3.2.5 there is no period P in the equations which is due to the parameter τ, being time measured in units of the outer orbital period. This problem is solved in the first two equations when deriving, but in the third there is still a missing parameter for the masses of the black holes and semi-major axis for the star and companion black hole defined by $\eta = m_\bullet\, m_c/(m_\bullet + m_c)^2$ and $\alpha = a_c/a_\star$. These parameters comes from the rescaled time τ:

$$\tau = \frac{t}{16}\,\eta\,\alpha^2\,\frac{2\,\pi}{P_2}. \tag{3.2.13}$$

Using equation 3.2.13, adjusting the notation to be compatible with Naoz et al. (2020) and using that equation 3.2.5 is in units of the period, equation 3.2.5 is found finally by combining equation 3.2.9 and 3.2.10 with 3.2.6.

The three equations 3.2.3, 3.2.2 and 3.2.5 describe how the system behaves and how the orbital plane are placed compared to the plane of reference.

The general relativistic (GR) precession effects on the orbit are given by equation 5 and 6 in Naoz et al. (2020) for the companion black hole and star respectively:

$$\left(\frac{d\varpi_c}{dt}\right)_{\text{GR}} = \frac{6\,\pi\,G\,m}{P_c\,c^2\,a_c\,(1 - e_c^2)}, \tag{3.2.14}$$

$$\left(\frac{d\varpi_\star}{dt}\right)_{\text{GR}} = \frac{6\,\pi\,G\,m}{P_\star\,c^2\,a_\star\,(1 - e_\star^2)}. \tag{3.2.15}$$

In order to arrive to equation 3.2.14 and 3.2.15 equation 25 from Naoz et al. (2017) is used:

$$\left.\frac{d\omega_1}{dt}\right|_{\text{GR,inner}} = \frac{3\,k^2\,(m_1 + m_2)^{3/2}}{a_1^{5/2}\,c^2\,(1 - e_1^2)} \tag{3.2.16}$$

In the chosen frame of reference, the inner orbit carry all the angular momentum, meaning that the inner orbit will be the rotating frame. Thus setting $\omega_1 = -\pi - \Omega_2$

then the GR precession of ω_1 can translate to a precession of Ω_2 which is defined by equation 26 in Naoz et al. (2017):

$$\frac{d\Omega_2}{dt}\bigg|_{\mathrm{GR},\Omega_2} = -\frac{3\,k^2\,(m_1 + m_2)^{3/2}}{a_1^{5/2}\,c^2\,(1 - e_1^2)}.\tag{3.2.17}$$

Equation 3.2.14 and 3.2.15 differ from equation 3.2.17 with the parameter k and G. The parameter k is the Gaussian gravitational constant and is defined as:

$$k = \frac{2\,\pi}{P}\sqrt{\frac{a^3}{m_1 + m_2}}.\tag{3.2.18}$$

The constant can be derived from Kepler's third law [8]

$$P^2 = \frac{a^3\,4\,\pi^2}{G\,(m_1 + m_2)}.\tag{3.2.19}$$

k^2 as often known as G, Newton's gravitational constant. Using G instead of k^2 and inserting equation 3.2.18 into equation 3.2.17, the equation 3.2.14 and equation 3.2.15 emerge.

The GR precession is important to consider since it tend to suppress the inner orbit eccentricity excitations which is associated with EKL mechanism, meaning it can suppress the flip of the orbital plane . This thesis deals with the secular case where the outer orbit is assumed to be a test particle and the inner orbit is massive, meaning that the outer orbit does not affect the inner orbit with its gravitational interactions. Though the outer orbit does not affect the inner orbit, the inner orbit can still precess due to GR with nominal precession rate, meaning that there must be a GR precession strong enough to supress the quadrupole excitations. Large eccentricity values can lead to instability by the star moving too close to the SMBH binary so it will experience a three-body scattering event [31].

In order to consider an upper limit for the mass range of the companion black hole including the precession of the star, equation 14 in Naoz et al. (2020) is investigated:

$$\frac{d\varpi}{dt}\bigg|_{\star} = \frac{6\,\pi\,G\,m_{\star}}{P_{\star}\,c^2\,a_{\star}\,(1 - e_{\star}^2)} + \frac{3\,\pi}{8}\,\eta\left(\frac{a_c}{a_{\star}}\right)^2\frac{\mathcal{S}\,P_{\star}^{-1}}{(1 - e_{\star}^2)^2},\tag{3.2.20}$$

where $\mathcal{S} = 4 + 6\,e_c^2 - 3\,Q\,\sin^2 i_\star$.

Equation 3.2.20 is found by combining equation 3.2.5 and 3.2.15. In equation 3.2.5 the term $(1 - \theta^2)$ can be written as $\sin^2 i_\star$ since $\theta = \cos i_\star$.

Equation 3.2.20 has been chosen to be exempted in the results, but this can be implemented in order to reduce the mass regime even further.

The next equation to find the upper limit from, is equation 13 from Naoz et al (2020):

$$\left|\frac{d\vec{j}}{dt}\right|_\star = \frac{3\,\pi}{4}\,\eta\,\left(\frac{a_c}{a_\star}\right)^2\,\frac{\sin i_\star}{(1 - e_\star^2)^2}\,\frac{\mathcal{R}}{P_\star}, \tag{3.2.21}$$

where $\vec{j}$ is the angular momentum unit vector $\vec{j} = (\sin i \sin \Omega - \sin i \cos \Omega, \cos i)$ and $\mathcal{R} = [Q^2 \cos^2 i_\star + 25\,e_c^4 \sin^2 2\omega_c]^{1/2}$.

To arrived at equation 3.2.21 equation 11 in Naoz et al. (2020) is used:

$$\left|\frac{d\vec{j}}{dt}\right|^2 = \left(\frac{d\theta}{dt}\right)^2 + \sin^2 i_\star \left(\frac{d\Omega}{dt}\right)^2 \tag{3.2.22}$$

By inserting equation 3.2.3 and 3.2.2 into equation 3.2.22 the above equation 3.2.21 is reached.

In both equation 3.2.21 and 3.2.20 the period is present. This is due to going from the time parameter τ which is measured in units of the period to the time t.

In this section a summary of how the Konzai-Lidov mechanism works has been given and how it can be applied to the work in this thesis.

The Konzai-Lidov mechanism can be applied using the equations in Section 3.2. These equations have been derived and their origin has been explained and how they work.

This leads to the next section where an explanation of how the different data for the orbital properties for the stars are obtained.

4 Observations

This section includes an explanation of the different observational methods used to obtain data for the orbital properties of the stars examined. These stellar properties are used to determine properties of Sgr. A*. Furthermore this section contains a summary of the different telescopes and instruments used in the observations to obtain the data. The data used in this thesis is obtained from Åkesson & Kristensen (2019) [18] and Peißker et al. (2020a) [32].

Åkesson & Kristensen (2019) use data from 7 different stars orbiting Sgr. A* and 4 different data points of S0-2. The data obtained in Åkesson & Kristensen (2019) is acquired using 5 different papers in which S0-2 is present in all, thus 4 different data points for S0-2 have been chosen. Data from Åkesson & Kristensen (2019) consists of orbital properties of the stars S0-1, S0-2, S0-16, S0-19, S0-20, S0-38 and S0-102. Peißker et al. (2020a) use data from 8 different stars orbiting Sgr. A*. The orbital properties obtained in Peißker et al. (2020a) consist of data from the stars S0-2, S0-19, S0-29, S0-38, S0-42, S0-60, S0-62 and S0-64. Data from S0-2, S0-19 and S0-38 are found in both set of data. A summary of which stars used in this work from the different observations can be found in Table 1. The data of the stars have been found using near infrared cameras, thus observed in the optical spectrum.

By using data from different stars orbiting Sgr. A* it is possible to study their behavior near the black hole. Their orbits and perturbations can lead to knowledge about the properties of the black hole they are orbiting, e.g. Sgr. A* or the companion black hole. A property could be the mass of Sgr. A* as found in Åkesson & Kristensen (2019) using Keplers third law. By considering the Roche Limit of Sgr. A* it is possible to determine if the stars are close enough to be consumed by the black hole or are in a safe distance.

4.1 Observational Methods

To better understand how the different instruments used in the observations work, the main techniques are described in this section.

4.1.1 Diffraction Limited Imaging

The fundamental limit on the telescope image quality is set by the wave properties of light. When the point source is very distant, its wavefronts will arrive at the telescope as plane or parallel surfaces. Even though the source is a point its plane waves will diffract when encountering the entrance aperture of the telescope. This produces an image of finite size. The size of the image is called the diffraction limit of the telescope which depends on the radius of the aperture and the wavelength of the incoming light. The image is a pattern of concentric bright rings with the majority of light focused into a disk, an airy disk. The disk has an angular radius α_A.
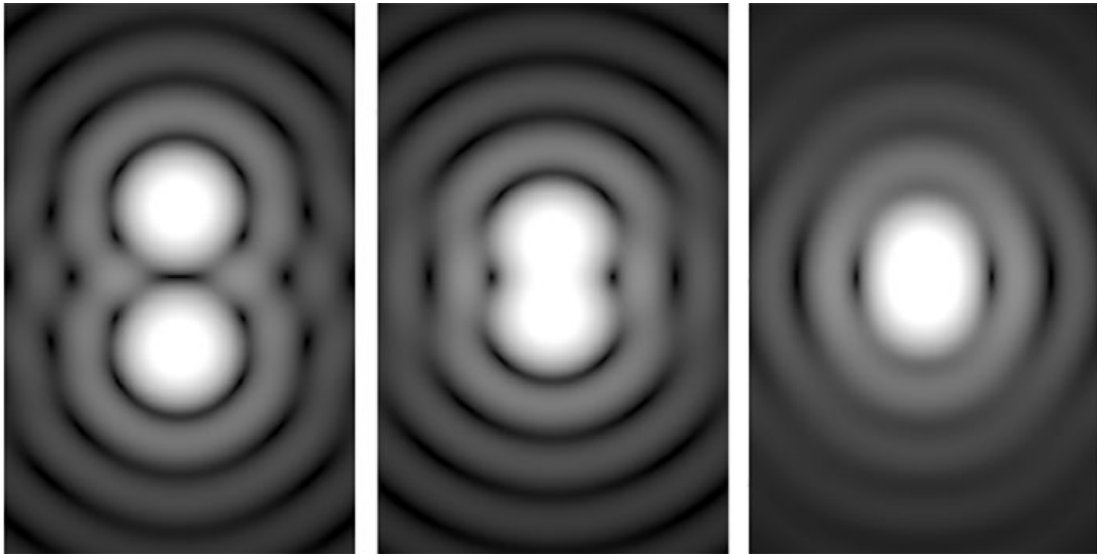

Figure 11: Illustration of the Rayleigh criterion. *Left*: The sources are farther apart than α_A. *Middle:* The sources meet at α_A. *Right:* The sources are closer than α_A. Figure from Physics World website [33].

It may not be possible to distinguish two point sources from each other if they lie close together due to their airy patterns blending. It is not possible to determine if it is one or two sources. To distinguish these from each other Rayleigh's criterion needs to be satisfied [34]. The criterion requires the distance between the center of the two airy discs must no be closer than α_A, given that they have the same radii. Figure 11 illustrate how the light source will be placed depending on α_A.

The resolution in diffraction limited imaging is only limited by the diffraction limit [34].

4.1.2 Speckle Imaging

While Rayleigh's criterion gives a good prediction of the performance of space telescopes, the telescopes on Earth have other problems to overcome, especially turbulence on the surface. The turbulence causes dynamic density variations in the atmosphere, which limits the resolution of all but the smallest telescopes. This phenomenon is called seeing.

If the conditions are ideal then the plane waves will diffract when entering the aperture of the telescope and focus as a airy pattern as described in section 4.1.1. When
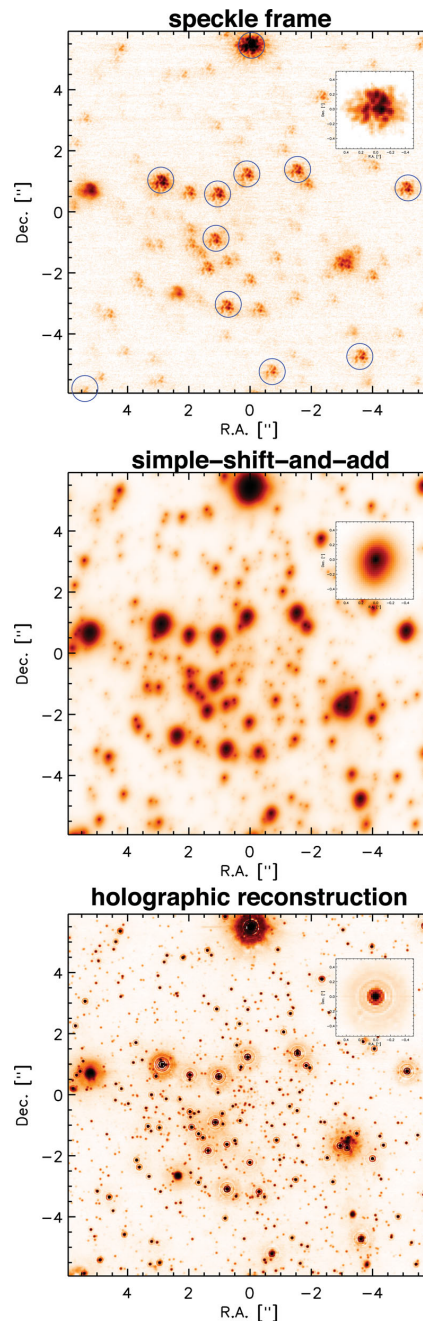

Figure 12: Speckle observations of the Galactic Centre. *Top*: Single speckle frame with reference stars used for reconstruction marked by circles. *Middle*: SSA image. *Bottom*: Holographic reconstruction. *Insets*: PSFs for each image. Figure 1 from Schödel et al. (2013) [37]

38

using Earth-bound telescopes the turbulent atmosphere will create "lumps" of air with refraction indices higher or lower than their surroundings. This will make the incoming plane wavefronts to retard some sections or speed up others. This results in a distorted front with different segments having slightly different directions in the focal plane. In the image each segment of the wavefront will be in different locations in the focal plane and thereby several airy disks will be produced. The combination of these airy patterns is called speckle pattern. An example on these speckle patterns can be found in Figure 12 in the top frame.

These patterns has only a momentary existence due to turbulence. The turbulence will move the lumps of air around very quickly and therefore it has a very short exposure time below about 1/20 second.

Using the technique speckle interferometry it is possible to recover the diffraction limited image by removing the interference effects. This technique requires a short exposure time which is only useful with bright objects and telescopes with a large aperture. The speckle pattern will produce a seeing disk if the exposure time is too long, due to the turbulence [34].

4.1.3 Speckle Holography Technique

In order to obtain more clear images a new technique has been evolved called Speckle Holography. In Boehle et al. (2016) they originally used a shift-and-add algorithm (SAA) to reduce their speckle images. In SAA only the brightest speckle from each frame contributes to the diffraction limited core of the final point-spread function (PSF) thus all remaining speckles are part of a substantial halo. In SAA each individual frame is shifted so the brightest pixel of each frame is in the same position before averaging the highest quality frames together.

By using the speckle holography technique instead it is possible to obtain a more sophisticated speckle reconstruction. The technique involves the deconvolution of observed, distorted images with the instantaneous PSF measured from a set of reference sources. Using this technique all the speckle information is contributing to the final diffraction-limited core. This results in a higher Strehl ratio, which

describes the quality of the image [36].

Figure 12 shows observations in the galactic centre. The top image shows a single speckle frame with reference stars. In the middle is the SAA image and in the bottom is the holography reconstruction. In each image their PSF have been inserted. A significant improvement can be seen using the holography technique.

4.1.4 Adaptive Optics

In order to correct the wavefront distortions from seeing, a technique called adoptive optics (AO) has been created. It uses a bright reference element next to the target, either a bright star or an artificial star. These artificial stars (Laser Guide Stars - LGS) are created by laser excitation of Sodium atoms in the upper atmosphere.

By inserting a reflective object near the focal point of the telescope it is possible to reduce the seeing and therefore distorted wavefronts by adjusting the shape of this element. This element, e.g. a deformable mirror compensate for the aberrations to the known reference object and are performed in real time with a feedback loop. This creates a longer exposure time and can create better images below the diffraction limit [6] [34]. In Figure 13 the technique is shown.

In Figure 14 the very noticeable effect of using adaptive optics can be seen. The figure shows observations of the galactic center with and without adaptive optics. In the left image the AO are not used and the galactic center is a complete blur, while on the right the center is much more clear and it is possible to distinguish between the different objects in the area. The AO technique is a revolutionary tool to enhance images and thus collect more precise and accurate data.
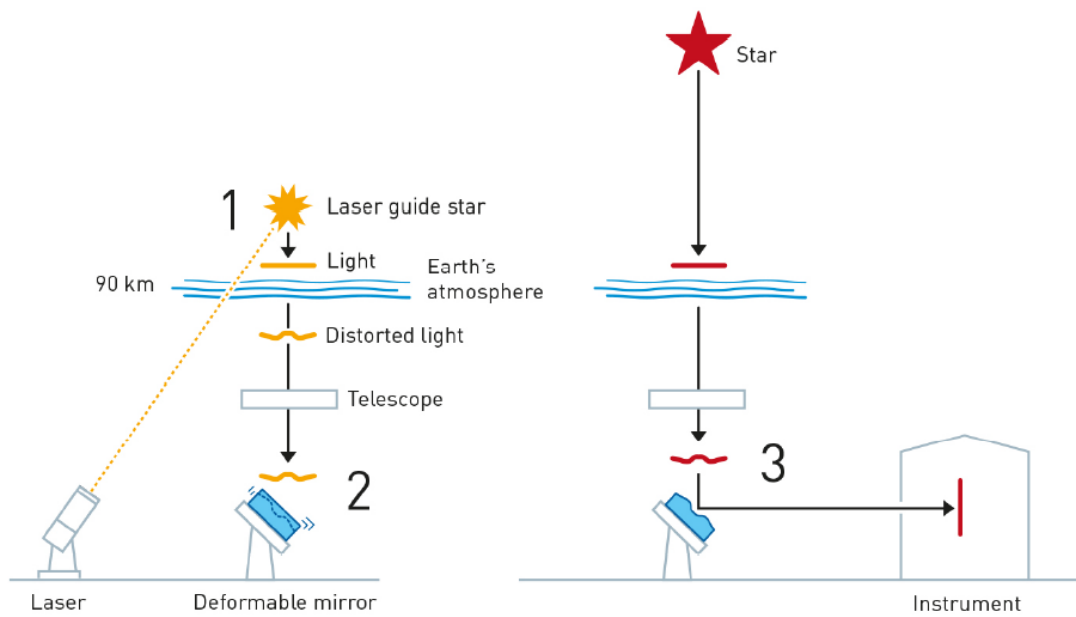
Figure 13: Principles of adaptive optics. The images of an artificial guide star made by the laser (1) are used in the feedback loop to introduce the fast changes of a mirror (2) that correct for the turbulence in the final science images (3). Figure 7 from Scientific Background on the Nobel Prize in Physics 2020 [6].
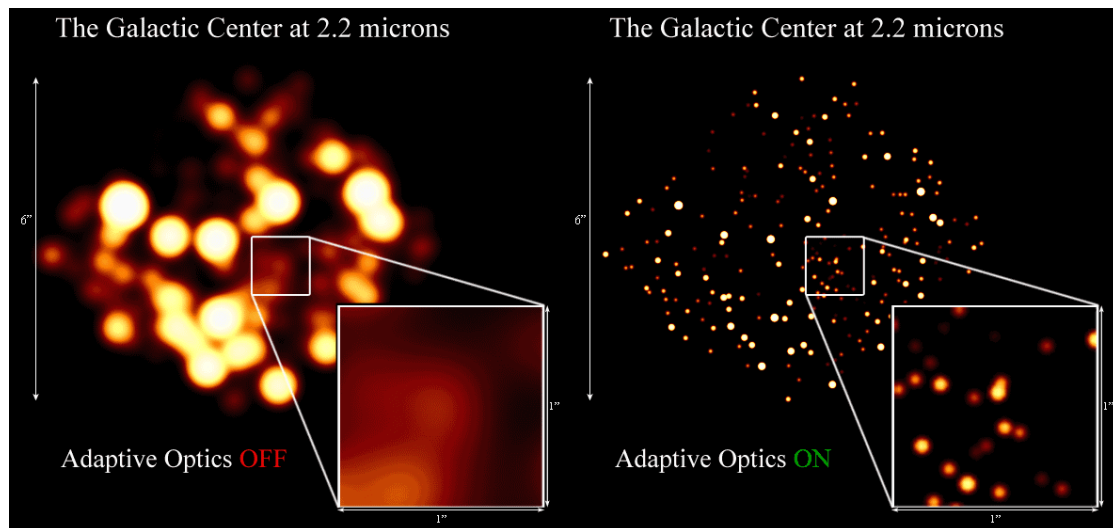

Figure 14: Observations of the Galactic Center with and without adaptive optics. Figure from UCLA Galactic Center Group [35]

4.2 Obtaining Data

Data of the stars S0-1, S0-2, S0-16, S0-19, S0-20, S0-38 and S0-102 obtained in Åkesson & Kristensen (2019) [18] have been used. The data have been obtained from five different scientific articles by Ghez et al. (2003 [38] and 2005 [39]), Meyer et al. (2012) [40], Boehle et al. (2016) [36] and Abuter et al. (2018) [41], respectively.

The stellar semi-major axes have been found using plots of the different stellar orbits from each article and then importing the plot into the graph digitizer *Get-Data*. The observational methods of the stellar orbits can be found in the following sections. The different plots of stellar orbits can be found in Figure 23, Figure 24, Figure 25, Figure 26 and Figure 27 in Appendix A.

Using the small angle formula [7], the results have been converted from arc sec into AU in order to have consistency in the units,

$$D = \alpha d,$$

where D is the linear size of the semi major axis in AU, α is the semi major axis in arc seconds, and d is the distance from earth to the centre of the galaxy in parsec. The distance d which has been used is: $d = 8.178 \pm 0.013_{stat} \pm 0.022_{sys}$ [42]. By combining the errors by adding them in quadrature the result is $d = 8.178 \pm 0.026$ kpc [18].

The inclination angle has not been taken into account in this data. The inclination angle describes how the orbital plane is placed compared to the plane of reference, thus the tilt of the orbit.

The different observational methods by which the data used in Åkesson & Kristensen (2019) have been obtained can be found in Sections 4.2.1, 4.2.2, 4.2.3 and 4.2.4. The observational method used in Peißker et al. (2020a) can be found in Section 4.2.5.

4.2.1 Ghez et al. (2003 & 2005)

The papers by Ghez et al. (2003) and Ghez et al. (2005) have used the same data set which is based on observations of the stellar cluster in the center of our Galaxy. The K(2.2μm)-band diffraction-limited speckle images have been obtained consistently by using NIRC (near infrared camera) on W.M. Keck I 10 m telescope from 1995-2004. The instrument was designed in order to produce both infrared images and low resolution spectra (1-5 micron) [43]. The data has been obtained from a 5" × 5" region centered on Sgr. A*. [38] [39].

On Maunakea on Hawaii the W. M. Keck Observatory is located. The observatory has two twin telescopes which are the most productive optical and infrared telescopes.
The location of the telescopes are not a coincidence. Hawaii is located in the middle of the Pacific Ocean, which is surrounded by thermally stable seas. The Maunakea summit is isolated and has no mountain ranges nearby to create a change in the atmosphere. The atmosphere above the summit is also very clear, calm and dry for most of the year which offers the best seeing on Earth. Hawaii is not densely populated so there is no significant light pollution in the night sky. These factors make the Keck Observatory an ideal place to observe the night sky. [44]

The primary mirror is 10 meter in diameter for each telescope and have a nanometer precision. The mirrors are composed of 36 hexagonal segments which work as a single piece of reflective glass.
The Keck I telescope began observations in May 1993 while the Keck II followed in October 1996.
The observations used are obtained in the infrared spectrum (1-5 micron) using NIRC1 & 2 [45].

4.2.2 Meyer et al. (2012)

The observations from Meyer et al. (2012) differ from Ghez et al. (2003 & 2005) by using AO, which improves the resolution of the imaging data.

Meyer et al. (2012) have obtained data using the W.M. Keck Observatory from 1995-2012 with speckle imaging and adaptive optics (AO). The speckle imaging was obtained from 1995-2005 with using NIRC on Keck I by capturing images of the center of the Galaxy on timescales of $\sim$ 0.1 sec. This is a short enough timescale to preserve the source's information since the exposure time is small compared to the coherence time of the atmospheric turbulence.

The observations with AO were carried out between 2004 and 2012 with NIRC2 on Keck II telescope. NIRC2 is an imager designed for the Keck adaptive optics system [46]. The observations are based on a laser guide star (LGS) generated with the Keck II sodium laser and corrections were determined from measurements of the natural guide star (NGS) USNO 0600-28577051 [40].

4.2.3 Boehle et al. (2016)

The data from Boehle et al. (2016) is based on three different types of data sets. The first data type is previously obtained speckle imaging data which has been re-reduced with the speckle holography technique. This results in deeper images in higher quality. The second type is new and previously reported data with AO astronomy, and the third type of data is new and previously reported AO spectroscopic data. The difference between the two AO data sets is that astronomy measures the positions of the stars while spectrometry measures the distribution of photons with wavelengths [18]. The previously reported data originate from previous work by Ghez et al. (2005), amongst others, which is not included in this thesis.

The speckle data is obtained between 1995 and 2005 from the same $\sim$ 5" $\times$ 5" central region as Ghez et al. (2003 & 2005), also with NIRC at Keck I telescope to obtain between 2000 and 20000 K(2.2μm)-band frames during each observation epoch with an exposure time of 0.1 sec.

The new AO data where obtained from 2012 and 2013 using the NIRC2 on the Keck II telescope. The new images are taken in the central $\sim$ 10" $\times$ 10" region of our Galaxy. The data were taken with an exposure time of 2.8 seconds. The

previously reported AO observations were obtained from 2004 through 2011. The data obtained from 2012 to 2013 are new high-resolution images compared to the previous reported data.

In May 2013 new spectroscopic data on S0-38 were obtained with OSIRIS (OH-Suppressing Infrared Imaging Spectrograph)[45] on the Keck I telescope with the AO system using the K(1.965-2.382μm)-broadband [36]. To provide images of different wavelengths, OSIRIS takes a small spectra in a small field of view. It is then possible to ignore wavelengths in which the atmosphere of the Earth brightly shine from the emission of OH molecules. Using OSIRIS allows astronomers to observe even fainter objects than previously possible [45].

4.2.4 Abuter et al. (2018)

The data from the K-band were obtained by speckle imaging and AO imaging from 1992 to 2018.

The sky-projected positions of S0-2 were obtained with the speckle camera SHARP at NTT (New Technology Telescope) between 1992-2002.

The New Technology Telescope is located in the Atacama Desert of Chile and Figure 15 shows the telescope in question. The NTT has a primary mirror at 3.58 meter in diameter and is very flexible and computer controlled. During observations the mirror's shape

Figure 15: The New Technology Telescope in Chile. Figure from ESO website. [48]

is adjusted by actuators which preserve the optimal image quality. The telescope operates in the optical and near infrared spectrum. [47]

In 1992 the SHARP I speckle camera was taken into use and since followed the SHARP II and SHARP II+ cameras with adaptive optics. SHARP is a near in-

frared camera build specifically to the NTT. It is a camera designed to obtain diffraction-limited images in the K-band of the galactic center [49] [50].

Most of the data is obtained from 2002-2018 with the AO-assisted NIR (Near infrared) imager NACO at VLT (Very Large Telescope) and the interferometric astronomy-imager GRAVITY with all four Unit Telescopes (UTs) of the VLT interferometer. The VLT is located in the Paranal Observatory in the Atacama Desert of Chile. The location of the Observatory is very isolated and far from any light pollution, which results in very dark nights. This is the facility for European ground-based astronomy.

It is an advanced optical telescope and it consists of four Unit Telescopes (UTs). The main mirror is 8.2 meters in diameter and it has four movable Auxiliary telescopes with a diameter of 1.8 meter. To create a huge interferometer, ESO Very Large Telescope Interferometer (VLTI), the telescopes can work together, making it possible to see a more detailed image than with the individual telescopes. The UTs are mostly used for individual observations, but are only available a limited number of nights a year for the interferometric observations, whereas the four Auxiliary telescopes are available for oberservations every night.

The telescopes operates in the optical spectrum, including the infrared spectrum, using interferometry.

The first of the UTs, called Antu, started operating in April 1999. Today all four of the UTs and Auxiliary telescopes are fully operational. The UTs are located in thermally controlled, compact buildings which synchronously rotate with the telescopes. The design of the buildings minimizes the obscuring effects the variation in weather can create, e.g. air turbulence in the telescope tube [51].

NACO is an instrument combined by two systems working together, NAOS+CONICA. NACO uses adaptive optics which enhance the images.

The first system is the Nasmyth Adaptive Optics System (NAOS). The AO system is equipped with both visible and infrared sensors. Due to flexible, computer controlled mirrors it can counteract the image distortions from atmospheric tur-

bulence in real time.

The second system is CONICA. It is an infrared camera and spectrometer which is attached to NAOS [52].

GRAVITY is an interferometer which combines the light of four VLT telescopes. This could be either the four UTs or the four Auxiliary telescopes, each assisted by AO.

Using this technique combining different telescopes, it is possible to observe faint objects. GRAVITY can be split in two interferometers, one stabilize the light of a bright star and uses this as a reference position in the sky. The second part can then observe the object of interest with long exposure times.

The instrument can correct even further for atmospheric turbulence due to having its own fringe tracker [53].

The SHARP/NACO data gives the relative positions between the stars and are registered with a precision of ≤ 1 mas in the radio frame of the galactic center. Further epochs of K- and H-band images have been added from May 2018. Additionally the radial velocity measurements of S0-2 are obtained by using SIN-FONI at the VLT and NIRC2 at Keck II from 1992-2018 [41].

4.2.5 Peißker et al. (2020a)

The data from Peißker et al. (2020a) is obtained by using NACO with the K-band filter and SINFONI at VLT.

The used LGS IRS7 from AO is located around 5".5 north of Sgr. A*. Each exposure consists of 3 integrations of 10 seconds each.

The data from SINFONI in this paper is downloaded from the ESO archive and are observed in the H+K grating [32].

SINFONI is located on one of the UTs. Similar to NACO it is two instruments combined. The first is the infrared integral field spectrograph, SPIFFI (SPectrometer for Infrared Faint Field Imaging) and second is the SINFONI-AO module which adjusts for the atmospheric turbulence.

Using an integral field spectrograph it is possible to observe in three dimensions across an astronomical object in one take. In the image, each pixel is associated with a full spectrum and by measuring the light intensity at each wavelength, it is possible to determine the relative position and velocity (either towards or away from Earth) of an object.

SINFONI uses a technique called the 'image slicer'. This technique places an array of n long, narrow mirrors stacked side by side in the x-direction in the two- dimensional image plane in a fashion so none of the slices overlap, then each mirror is tilted in a different direction. Each mirror will act like a slit, so each mirror's 'slice' of the image will be reformed on the spectrograph's slit. Every slice will be displace in the y-direction, so none of the slices overlap. It is then possible to reconstruct the image from all the individual slices and combine it to a 3-dimensional image [34] [54].
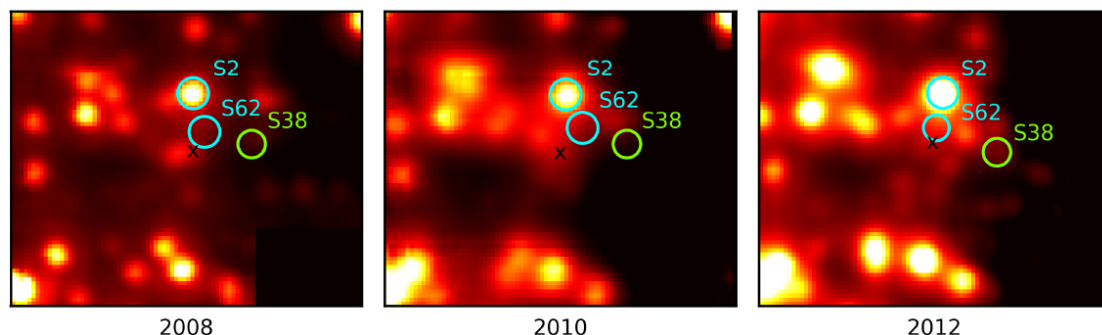

Figure 16: K-band images from SINFONI from 2008-2012. The black X marks the position of Sgr. A*. Figure 11 from Peißker et al. (2020a) [32].

In Figure 16 data of the star S0-62 can be seen. The data have been collected using SINFONI from 2008-2012. The star S0-2 has a fixed position and Sgr. A* is marked with a black X. It is possible to see how close the different stars orbit each other and it is hard to distinguish them from each other [32].

In Figure 17 the orbit of S0-62 can be found marked as the red orbit. Peißker et al. (2020a) have obtained their starting value by varying the right ascension (R.A.) and declination (DEC.) value of their measured positions by ± 6.5 mas and then averaging the results to determine 1σ uncertainty. The orbit of S0-62 is highly eccentric, so the observations can easily be confused with the orbit of S0-2. S0-62

is only observable after the periapse of S0-2 in a time period of around 11 years. Its orbit will blend with S0-2 during the periapse of S0-2. [32] The period of the star is much shorter than S0-2 and only 9.9 years compared to S0-2 with a period of 16 years [32] [18].
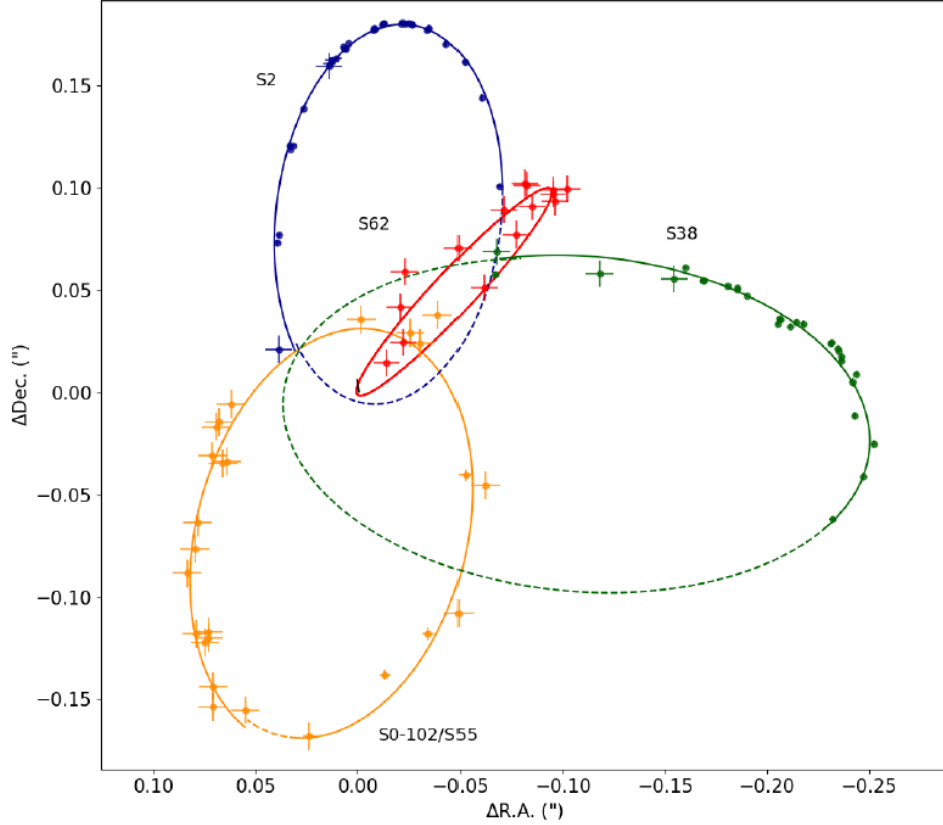

Figure 17: Orbits of S0-2, S0-62, S0-38 and S0-102. Sgr. A* is located at the origin of the coordinate system, marked with the black line at RA: 0.0", DEC. 0.0". Figure 3 from Peißker et al. (2020a) [32]

4.3 Evolution in Technology

Technology has evolved rapidly through the past 20 years, which can be seen in the instruments used in the different telescopes. By improving the technology, better and more accurate data can be obtained which can be seen in the different data sets throughout the years.

In the following sections the different instruments and telescopes will be evaluated

in comparison with each other in order to determine which gives the most accurate data.

4.3.1 Keck Telescopes

The Keck I and II telescopes have evolved since they first saw the light of day in 1993 and 1996, respectively. The most groundbreaking upgrade was installing AO technology in 1999 on Keck II and later using LGS AO in 2004 on both Keck telescopes [44]. The AO technique allows for better images in higher resolution than before.

Another upgrade in technology is using the NIRC2 instead of NIRC. The NIRC2 was designed for the AO technology and therefore enhances the images obtained with the near-infrared camera. In 2010 NIRC retired from service in order to make room for new instruments [55].

4.3.2 Evaluation of the Different Telescopes

The three telescopes presented in this section are the Keck telescopes, the Very Large Telescope (VLT) and the New Technology Telescope (NTT). But which one is better? In the previous subsection the evolution of the Keck telescopes has been described, but can it keep up with NTT and VLT?

The newest data is obtained by VLT and NTT telescopes with the instruments SHARP, NACO, GRAVITY and SINFONI.

Abuter et al. (2018) used different instruments in order to obtain data for the stellar properties. Figure 18 shows the different data. The plot on the left hand side shows a complete orbit of S0-2 with data points from SHARP (triangles), NACO (circles) and GRAVITY (squares) color-coded by time. The data has been improved throughout the years as the instruments also have improved. In the 1990's SHARP had a $\approx$ 4 mas precision, in the 2000's NACO had $\approx$ 0.5 mas precision and in 2018 GRAVITY had a precision as small as $\approx$ 3 μas. In the right bottom image a zoom in of the pericenter of the orbit is shown, which shows just how precise the measurements are with GRAVITY. NACO could detect the motion of
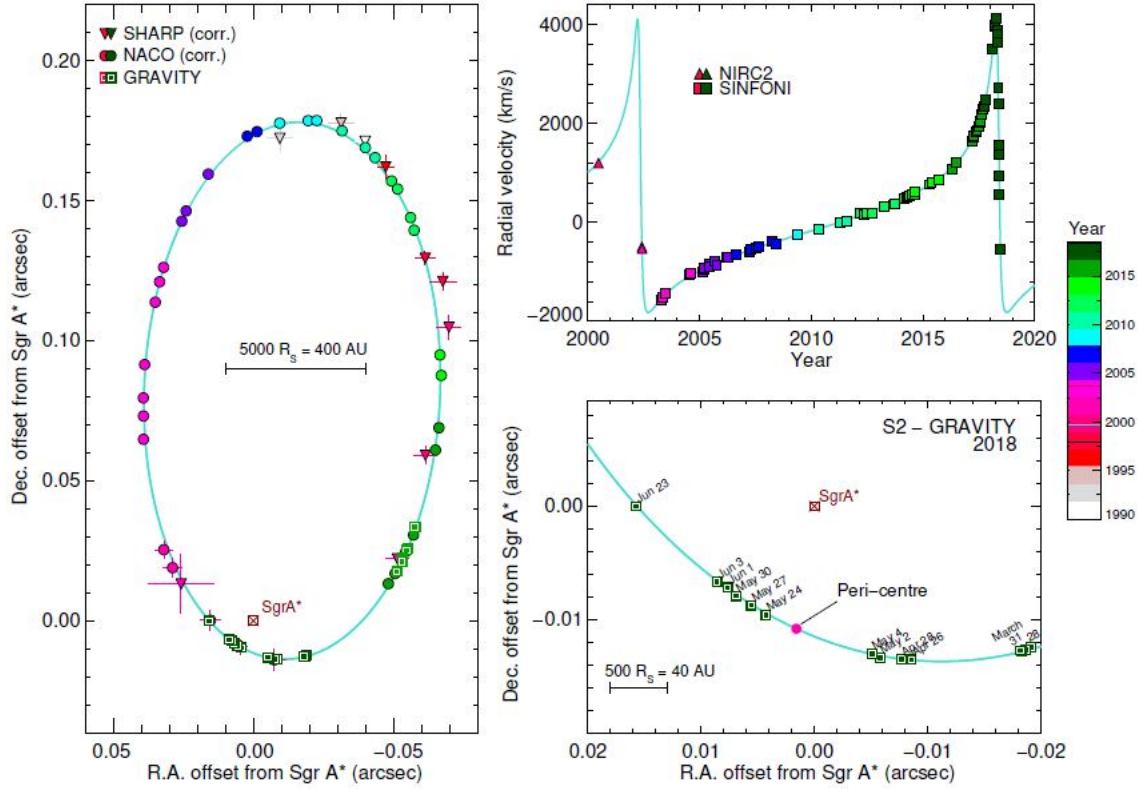
Figure 18: A summary of the observational results from Abuter et al (2018) by monitoring the orbit of S0-2 in the vicinity of Sgr. A* from 1992 to 2018. *Left*: Projected orbit of S0-2. Triangles represent SHARP data, circles NACO data and squares GRAVITY. The observations are color-coded for time. The best-fitting orbit of S0-2 is shown with the cyan curve. *Right top*: Radial velocity of S0-2 as function of time in years. The dips ind the plot around 2002 and 2018 represent when S0-2 reached pericenter of its orbit. Triangles represent NIRC2 data and squares SINFONI. *Right bottom*: A zoom in around the pericenter in 2018. Figure 2 from Abuter et al. (2018) [41].

S0-2 over a month while observations with GRAVITY could detect the motion from day to day, which is significant improvement. [41] The improvement can be seen in the interval between the data point on the left hand side figure. The errors on the SHARP data are larger than on the NACO and GRAVITY data and they do not fit as well on the curve of the orbit.

On the top right image the radial velocity of S0-2 is shown as a function of time in years. The measurements are obtained with NIRC2 on the Keck II telescope and SINFONI on VLT in a period from 1992 to 2018. In 2004 SINFONI first saw the

light of day and then replaced the NIRC2 [54]. The dips in the figure show when S0-2 have reached the pericenter of the orbit in 2002 and 2018 [41].

In Table 1 a summary of the different telescopes and instruments used to observe the different stellar orbits can be found. The different groups have all used AO except Ghez et al. (2003 & 2005) [38][39].

	Telescope	Instrument	Stars observed
Ghez et al. (2003 & 2005)	Keck I	NIRC	S0-1, S0-2, S0-16, S0-19, S0-20
Meyer et al. (2012)	Keck I & II	NIRC 1 & 2	S0-2, S0-102
Boehle et al. (2016)	Keck I & II	NIRC 1 & 2, OSIRIS	S0-2, S0-38
Abuter et al. (2018)	NTT, VLT	SHARP, NACO, GRAVITY	S0-2
Peißker et al. (2020a)	VLT	NACO, SINFONI	S0-2, S0-19, S0-29, S0-38, S0-42, S0-60, S0-62, S0-64

Table 1: Table of the different telescopes and instruments the different groups have used on the different observations. A0 is used in all observations, except Ghez et al. (2003 & 2005).

This section has explained how the different stellar properties have been obtained, how the different instruments and observational methods work. Furthermore a discussion on how the different instruments have evolved have been included. This leads to the next section which shows the data obtained in Åkesson & Kristensen (2019) and Peißker et al. (2020a). This data is used in the methods shown in Section 3 and used to work further on narrowing the mass regime in which the companion black hole exists in.

5 Data

In this section the data obtained in Åkesson & Kristensen (2019) [18] and Peißker et al. (2020a) [32] is presented.

The period and semi-major axes from different stars obtained in Åkesson & Kristensen (2019) can be found in Table 2. The semi-major axes obtained in Peißker et al. (2020a) can be found in Table 3.

5.1 Data from Åkesson & Kristensen (2019)

The semi-major axes and periods obtained in Åkesson & Kristensen (2019) [18] can be found in Table 2. The obtained data originate from five different papers, and which stars originate from which publication can be found in detail in the table.

In Table 2 some data are from Ghez et al. (2005) and Boehle et al. (2016). This is due to missing data in the other papers. For example, in Ghez et al. (2003) the data for the period of S0-1 is missing, but in order to use the period for further work, the data for the period is obtained from Ghez et al. (2005) and the same is the case with Boehle et al. (2016). For S0-2 from Abuter et al. (2018) the error on the period is obtained from Boehle et al. (2016). The data from Boehle et al. (2016) has been chosen since it is closer to observational methods from Abuter et al. (2018) than Ghez et al. (2005).

The main difference between the data from Ghez et al. (2005) and Boehle et al. (2016) is the improvement in their observational instruments and techniques. Further explanation can be found in Section 4.

Star	Semi-major axis, 10^3 [AU]	Period [yr]
S0-1 (Ghez 2003)	2.85 ± 0.09	$190^* \pm 180^*$
S0-2 (Ghez 2005)	0.75 ± 0.08	14.53 ± 0.65
S0-2 (Meyer 2012)	0.84 ± 0.08	$14.53^* \pm 0.65^*$
S0-2 (Boehle 2016)	0.81 ± 0.08	15.9 ± 0.04
S0-2 (Abuter 2018)	0.79 ± 0.04	$16.05 \pm 0.04^{**}$
S0-16 (Ghez 2005)	1.58 ± 0.08	36 ± 17
S0-19 (Ghez 2005)	1.75 ± 0.08	37.3 ± 0.38
S0-20 (Ghez 2005)	1.83 ± 0.09	43 ± 45
S0-38 (Boehle 2016)	1.17 ± 0.08	19.1 ± 0.6
S0-102 (Meyer 2012)	0.88 ± 0.08	11.5 ± 0.3
Weighted mean for S0-2	0.78 ± 0.03	15.97 ± 0.03

Table 2: The semi-major axis obtained in Åkesson & Kristensen (2019) [18]. The * denotes data used from Ghez et al. (2005), and ** marks data from Boehle et al. (2016).

The weighted means for the semi-major axis and period have been determined using error propagation [56]:

$$\bar{\mu}_i = \frac{\sum_{i=1}^{N} x_i\, w_i}{\sum_{i=1}^{N} w_i}, \tag{5.1.1}$$

where $w = 1/\sigma_i^2$. The weighted error is determined by:

$$\sigma_{\bar{\mu}_i} = \sqrt{\frac{1}{\sum_{i=1}^{N} w_i}}. \tag{5.1.2}$$

The weighted mean has been found using the four different data points for the semi-major axis and period for S0-2.

5.2 Data from Peißker et al. (2020a)

Data from Peißker et al. (2020a). The data has been converted from mpc to 10^3 AU using the build-in unit converter in Maple 2021 [2].

---

[2] https://www.maplesoft.com/

Star	Semi-major axis, 10^3 [AU]
S0-2	1.04 ± 0.003
S0-19	2.38 ± 0.41
S0-29	5.92 ± 0.53
S0-38	1.16 ± 0.04
S0-42	7.96 ± 0.57
S0-60	4.20 ± 0.66
S0-62	0.74 ± 0.003
S0-64	3.28 ± 0.56

Table 3: Semi-major axes from Peißker et al. (2020).

The data in table 2 and 3 are used in further work in the results, which can be found in section 6. The semi-major axes for the different stars have been plotted in order to obtain an upper limit for the semi-major axis of the companion black hole.

6 Results

This section contains a presentation of the obtained results. Different data has been used in order to reduce the allowed mass regime of the companion black hole to exist in.

6.1 Background for Plotting

In order to obtain an upper limit for the companion black hole different functions have been used.

The first is the timescale associated with gravitational damping on the inner orbit [28]:

$$t_{GW} \sim 2 \times 10^8 \, \text{yr} \left(\frac{4 \times 10^6 \, \text{M}_\odot}{m_\bullet} \right) \left(\frac{10^4 \, \text{M}_\odot}{m_c} \right) \times \left(\frac{m}{4 \times 10^6} \right)^{-1} \left(\frac{a_c}{100 \, \text{AU}} \right)^4 \quad (6.1.1)$$

This describes the region of the merger time of gravitational waves. Only a merger time up to 10 Myr is under consideration. The grey region in the figures in this section denotes this area.

The semi-major axs found in Table 2 and 3 have been plotted in order to reduce an upper limit for the semi-major axis of the companion black hole.

Furthermore to obtain the upper limit the function for angular momentum's variation over time is implemented:

$$\left| \frac{d\vec{j}}{dt} \right|_\star = \frac{3\pi}{4} \eta \left(\frac{a_c}{a_\star} \right)^2 \frac{\sin i_\star}{(1 - e_\star^2)^2} \frac{\mathcal{R}}{P_\star} \quad (6.1.2)$$

This work uses the same bounds as Naoz et al. (2020) in equation 6.1.2: $i_\star = \Omega_\star = 45°$. I use $e_c = 0$ and $e_c = 0.9$ as the eccentricities for a circular orbit and a highly eccentric orbit of the companion black hole. The eccentricity of the orbit is now known, thus I have chosen to consider two scenarios. I have used the same data as Naoz et al. (2020) for S0-2 with $a_\star = 1020$AU, $e_\star = 0.88$ and $P_\star = 15.8$

years in order to use their results in comparison and for further work.

A mass of $4 \cdot 10^6 \mathrm{M}_\odot$ for Sgr. A* is assumed [28].

In order to find the pericenter angle for the companion black hole, the relation $\omega_c = \varpi_c - \Omega_\star - \pi$ is utilized. Like Naoz et al. (2020), it is assumed that $\varpi_c = 0$ so $\omega_c = -\Omega_\star - \pi$. $\Omega_\star$ is in degrees and in order for consistency between units then $\pi = 180°$.

In the next sections the results obtained using different semi-major axis in order to limit the allowed mass regime for the companion black hole will be presented. All figures can be found in a larger size in Appendix C.

6.2 Results Using Only Data from Åkesson & Kristensen (2019)

In Figure 19 the upper limit of the black hole mass must be under $10^5 \mathrm{M}_\odot$ otherwise it will enter the grey region for gravitational wave damping, which will be possible to detect. In this area the mass and semi-major axis of the companion black hole will be too close and it will be in danger of merging within 10 Myr.

The maximum mass for a circular orbit ($e_c = 0$) are $\approx 6.5 \cdot 10^4 \mathrm{M}_\odot$ with a semi-major axis of $\approx 150 \mathrm{AU}$.

The maximum mass for a highly eccentric orbit ($e_c = 0.9$) are $\approx 3.1 \cdot 10^4 \mathrm{M}_\odot$ with a semi-major axis of $\approx 115 \mathrm{AU}$.

The mass of the black hole can be in the allowed region with an upper limit of smallest semi-major axis of the star subtracted its periapse distance. Here is used the weighted mean for S0-2 as the value for the semi-major axis and the eccentricity found in Table 4:

$$r_p = a\,(1 - e) = (92 \pm 4)\,\mathrm{AU} \tag{6.2.1}$$

By subtracting this value from the semi-major axis of the weighted mean of S0-2, an upper limit for the semi-major axis of the companion black hole is found and can be seen as the black dashed line.

For simplicity I assume that the Roche limit of the black hole is be equal to the periapse distance and find the value of $a_c(\text{max}) \approx (702 \pm 30)$ AU.

The maximum mass with a semi-major axis of $a_c(\text{max})$ is $\approx 3.0 \cdot 10^3 M_\odot$ for a circular orbit and $\approx 0.8 \cdot 10^3 M_\odot$ for a eccentric orbit.
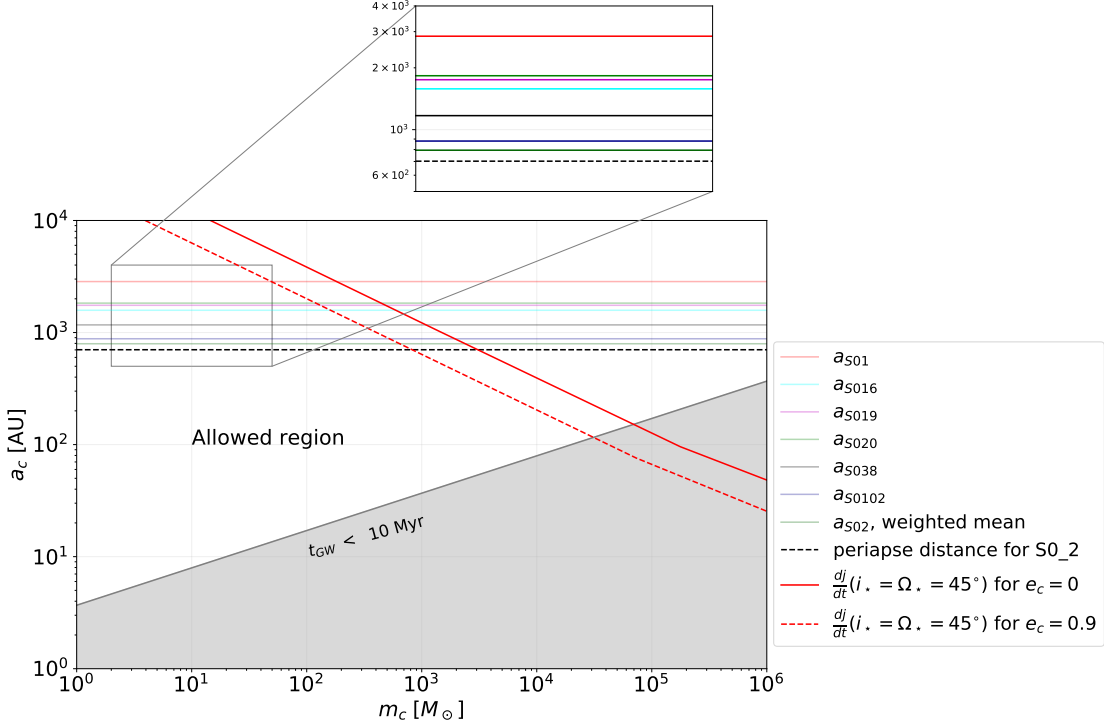

Figure 19: Results with data from Åkesson & Kristensen (2019). Plotted are the semi-major axes for the different stars, the timescale t_{GW} and dj/dt for $e_c = 0$ and $e_c = 0.9$

6.3 Results Using Only Data from Peißker et al. (2020a)

The upper limit for the mass are the same as for Åkesson & Kristensen (2019). It is only the masses of the upper limit of the maximum semi-major axis which are changed.

The periapse distance for S0-62 is calculate in the same manner as before and results in $r_p \sim (17.8 \pm 1.5)$ AU.

This gives a maximum allowed semi-major axis of $\approx (722 \pm 3)$ AU which is larger than the maximum allowed semi-major axis for Åkesson & Kristensen (2019).

58

At this value the maximum mass is $\approx 2.8 \cdot 10^3 \mathrm{M}_\odot$ for at circular orbit and $\approx 0.75 \cdot 10^3 \mathrm{M}_\odot$ for a eccentric orbit.
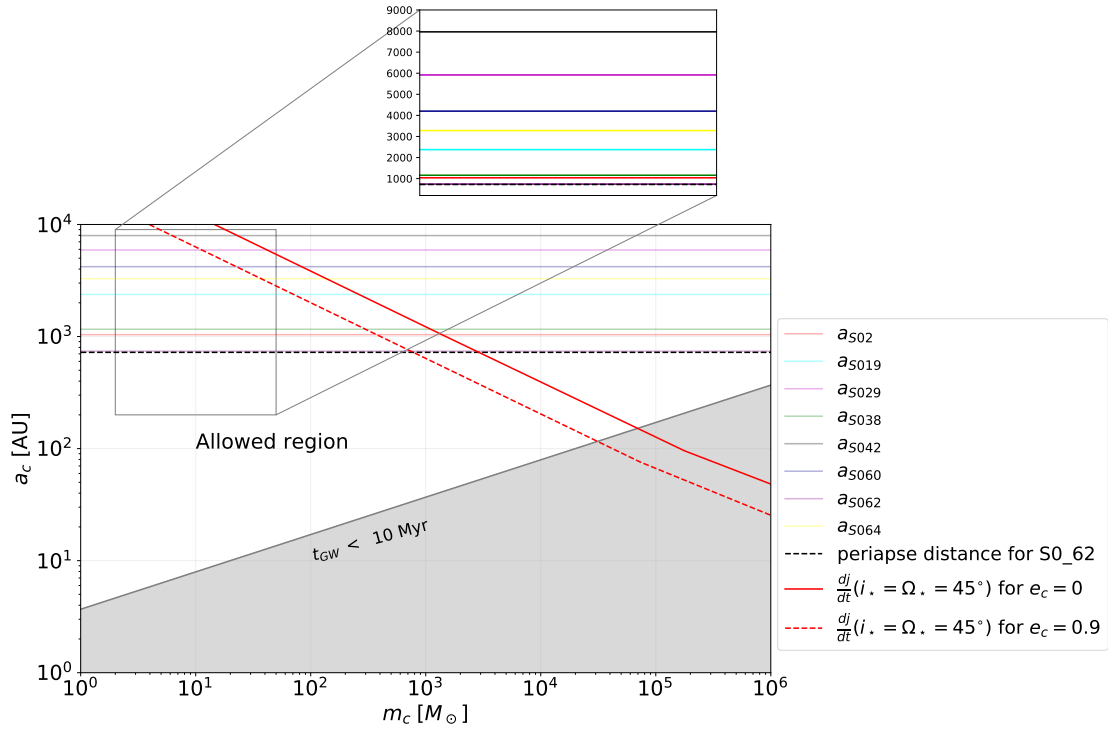

Figure 20: Results with data from Peißker et al. (2020a). Plotted are the semi-major axs for the different stars, the timescale t_{GW} and dj/dt for $e_c = 0$ and $e_c = 0.9$

7 Discussion

In this section a discussion of the results aloong with ideas to improve any future work is presented.

7.1 Improvement of Mass Region by Using More Stellar Orbits

By using more properties for stellar orbits in a closer orbit to Sgr. A* the possible semi-major axis of the companion black hole has been reduced.
Since the stars orbiting Sgr. A* are not being torn apart, then they must also be in a safe distance from the companion black hole.
Of all of the stars used, S0-62 has the closest orbit to Sgr. A* of $\approx (0.74 \pm 0.003) \cdot 10^3$ AU.
This is a significant improvement from Naoz et al. (2020) who use a semi-major axis for S0-2 of $1.02 \cdot 10^3$ AU. Further more Naoz et al. (2020) has an upper mass limit of 10^5 M$_\odot$ for a circular orbit with a semi-major axis of the companion black hole of 170 AU.
Using S0-2, the upper limit is found to be $6.5 \cdot 10^4$ M$_\odot$ for a circular orbit with $a_c = 150$ AU, which is significantly lower than Naoz et al. (2020).

7.2 Old vs. New Data on S0-2

In Figure 21 the data for S0-2 and S0-62 are combined.
They main difference in the data from Åkesson & Kristensen (2019) and Peißker et al. (2020a) is the inclination angle of the orbit. This is only considered in the data from Peißker et al. (2020a).

The semi-major axis for S0-2 from Peißker et al. (2020a) is denoted with the cyan colored line and is far above the other semi-major axis from Åkesson & Kristensen (2019). These semi-major axes are closer to S0-62 and their values are lower.
In Figure 16 it can be seen that the orbits of S0-2 and S0-62 are close, but they

should not be almost the same value.

It is safe to conclude that the inclination angle is an important factor when determining the semi-major axis of stellar orbits.
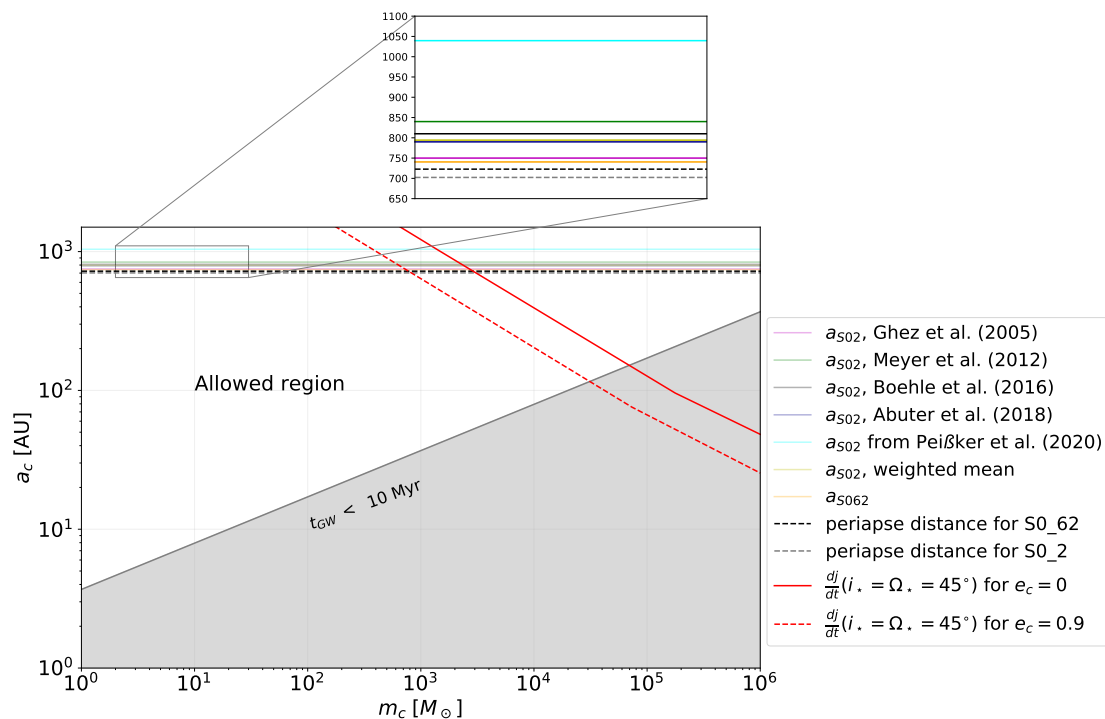

Figure 21: Results with data of S0-2 from Åkesson & Kristensen (2019) including the weighted mean, data of S0-2 and S0-62 from Peißker et al. (2020a). Plotted are the semi-major axes for the different stars, the timescale t_{GW} and dj/dt for $e_c = 0$ and $e_c = 0.9$.

7.3 Precision of Stellar Orbits

Even though S0-62 has a smaller orbit and is closer to Sgr. A* it does not have the most precise orbit.

S0-2 is well studied and have been observed for a full orbit. The full orbit of S0-62 has not been completely observed due to the orbit of S0-2 having blurred the view, which is described more in detail in Section 4.2.5.

In the future it might be possible to observe the orbit of S0-62 better and then get better data.

In any future work though, it is recommended to choose to work with S0-2 over S0-62, because it is well observed.

7.4 Possibility of Finding an Even More Accurate Mass Regime

It is possible to narrow the mass regime even further. In order to do this data for the stars S0-2 and S0-62, which have well defined properties, should be used. Based on this work, the data suggested to continue working with would be that originating from Peißker et al.(2020a & 2020b) [32][57] and Habibi et al. (2017)[58]. The value for the period of S0-2 is the weighted mean from Åkesson & Kristensen (2019) [18].

	S0-2	S0-62
$m_\star$ [$M_\odot$]	$13.6^{+2.2}_{-1.8}$***	6.1^{+2}_{-1}**
$P_\star$ [years]	15.97 ± 0.028	9.9 ± 0.02*
$e_\star$	0.884 ± 0.002*	0.976 ± 0.002*
$\Omega_\star$ [degress]	234.5 ± 1.03*	122.6 ± 0.01*

Table 4: Data for S0-2 and S0-62 used in the results. Data denoted with * is from Peißker et al. (2020a) [32], data denoted with ** is from Peißker et al. (2020b) [57], data denoted with *** is from Habibi et al. (2017) [58].

Inserting these values into equation

$$\left| \frac{d\vec{j}}{dt} \right|_\star = \frac{3\pi}{4} \eta \left(\frac{a_c}{a_\star} \right)^2 \frac{\sin i_\star}{(1 - e_\star^2)^2} \frac{\mathcal{R}}{P_\star} \tag{7.4.1}$$

and solving for the upper limit for the companion's semi-major axis, would most likely move the limits even further to the left, which will reduce the allowed regime. Furthermore, using even more stars in a closer orbit to Sgr. A* than S0-2 and S0-62 would reduce the regime even more. As we develop more accurate telescopes and instruments, it will be possible to obtain even better data and thus reducing the region further.

Another approach to getting a more accurate mass regime is to compare the periapse distance of the stars in orbits closest to Sgr. A* and thus to the companion black hole. By calculating this distance and comparing it to an approximated Roche limit of the companion black hole it is possible to determine an upper limit for the semi-major axis. If the periapse distance of the star is equal to or smaller than the Roche limit of the black hole, then the star will be torn apart of the tidal forces from the black hole.

To determine the Roche limit, it is necessary to calculate the radius of the star. This can be done, if there is any information available concerning the temperature of the star or which type of star it is.

Finally, by implementing equation 14 from Naoz et al. (2020) it would be possible to obtain an upper limit, when considering the precession of the star:

$$\left.\frac{d\varpi}{dt}\right|_{\star} = \frac{6\,\pi\,G\,m_{\star}}{P_{\star}\,c^2\,a_{\star}\,(1-e_{\star}^2)} + \frac{3\,\pi}{8}\,\eta\,\left(\frac{a_c}{a_{\star}}\right)^2\,\frac{\mathcal{S}\,P_{\star}^{-1}}{(1-e_{\star}^2)^2}, \qquad (7.4.2)$$

This is outside the scope of this thesis, but is definitely an idea to examine.

7.5 Observing the Companion Black Hole

At the moment it is not possible to observe the companion black hole - given that it exists.

If it exists, it will emit gravitational waves as the black hole binary moves and affects each other. This can potentially be detected by LISA. LISA (Laser Interferometer Space Antenna) is a space-based gravitational wave observatory. The detector will be consisting of three spacecrafts, separated by millions of miles.

LISA works in the low frequency range between 0.1 mHz and 1 Hz, where the groundbased LIGO works in frequencies between 10 Hz to 1000 Hz.

The waves LISA can detect have longer wavelengths which corresponds to objects in wider orbits and possibly heavier than LIGOs searching range. This gives the opportunity of detecting a wider range of gravitational wave sources [59].

As seen in Figure 22, it is possible for space based interferometers to detect compact binaries in our Galaxy and binary supermassive Black holes in the galactic nuclei.

LISA is first scheduled to launch in the early 2030's, so patience is necessary in order to observe the galactic center and find evidence of a binary black hole system.
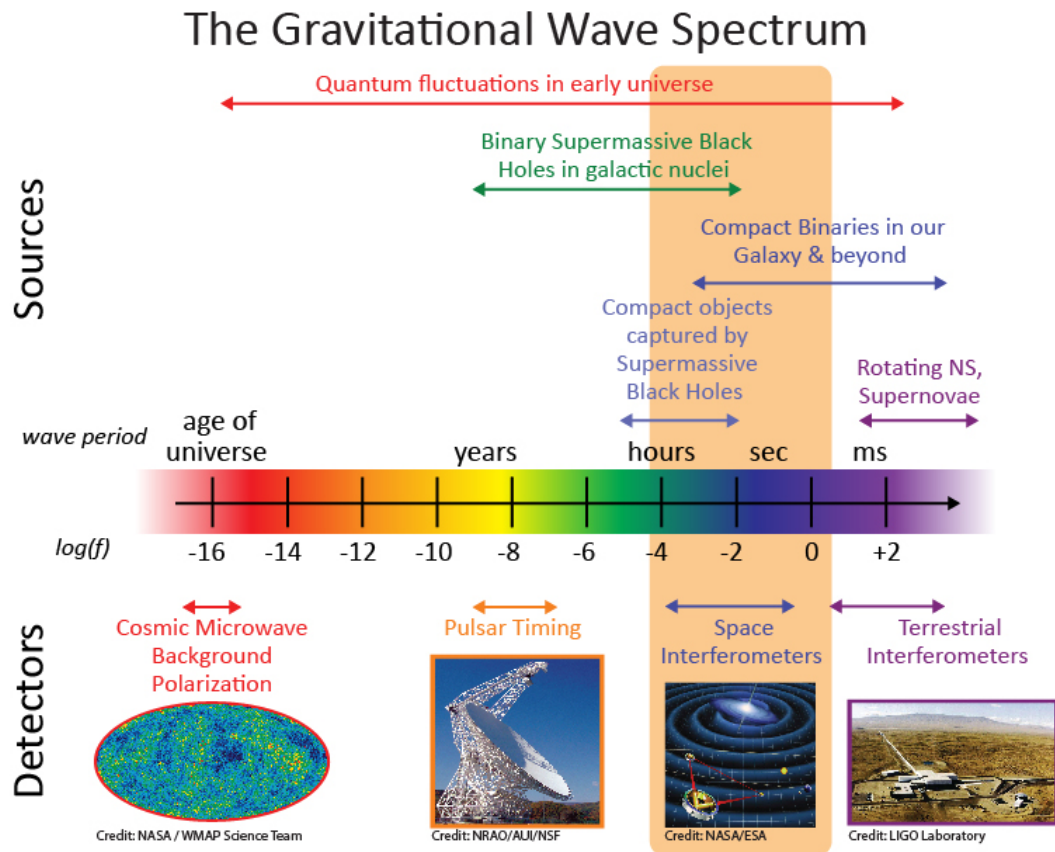

Figure 22: Gravitational wave spectrum with sources and detectors. Figure from LISA website [59].

8 Summary and Conclusion

This thesis has investigated a potential binary black hole system in the galactic center of the Milky Way Galaxy. In order to understand how such a system work the basics of black holes in general have been covered. These dense regions are an interesting subject to study and a lot of progress have been made during the past decades.

In the Universe it is very common to encounter three body systems. It is known that several stars orbit Sgr. A* and this work further assumes that Sgr. A* is part of a binary black hole system. Thus it was possible to examine Sgr. A* as actor in a triple system with two black holes and a star. This assumed triple system consists of a tight inner binary by Sgr. A* and the companion black. A star forms a much wider orbit around the black holes.

When assuming a triple system the Konzai-Lidov mechanism can be applied. The theoretical equations which follow the Konzai-Lidov mechanism have been derived and then implemented in the search for a reduced mass regime and to obtain an upper limit.

This thesis have expanded the work of Naoz et al. (2020) by using more orbital properties of stars in the vicinity of Sgr. A*. By using more stars the maximum allowed semi-major axes of the companion black hole's orbit have been reduced and following this, the mass regime has been reduced too.

Naoz et al. (2020) ruled out a black hole of a mass of $10^5 M_\odot$ in a circular orbit around Sgr. A* with a semi-major axis of 170 AU. This work reduces it even further to a maximum mass of $\sim 6.5 \cdot 10^4 M_\odot$ with a semi-major axis of 150 AU. For a highly eccentric orbit the mass is reduced to $\sim 3 \cdot 10^4 M_\odot$ with a semi-major axis of 115 AU.

Assuming that the companion black hole has a maximum semi-major axis corresponding to the semi-major axis of the star subtracted the stars periapse distance results in the masses being reduced even further. The maximum mass the com-

panion black hole can have with a maximum semi-major axis is determined to be in the range of 0.75 to 3 $\cdot 10^3 M_\odot$, depending on the eccentricity of its orbit.

A summary of the results using data from both Åkesson & Kristensen (2019) and Peißker et al. (2020) can be found in Table 5.

Åkesson & Kristensen (2019)	a_c [AU]	$M(max)$ [M$_\odot$]	$a_c(max)$ [AU]	M [M$_\odot$]
$e_c = 0$	150	$6.5 \cdot 10^4$	702 ± 30	$3.0 \cdot 10^3$
$e_c = 0.9$	115	$3.1 \cdot 10^4$	702 ± 30	$0.81 \cdot 10^3$
Peißker et al. (2020)	a_c [AU]	$M(max)$ [M$_\odot$]	$a_c(max)$ [AU]	M [M$_\odot$]
$e_c = 0$	150	$6.5 \cdot 10^4$	722 ± 3	$2.8 \cdot 10^3$
$e_c = 0.9$	115	$3.1 \cdot 10^4$	722 ± 3	$0.75 \cdot 10^3$

Table 5: A summary of the results using data from Åkesson & Kristensen (2019) and Peißker et al. (2020). The maximum mass and corresponding semi-major axis can be found in the table along with the maximum semi-major axis with corresponding mass for both a circular and eccentric orbit.

The mass regime can potentially be reduced by introducing more stellar properties of stars in closer orbit of Sgr. A* and thus allowing for making the constraints even tighter, e.g. properties of S0-62 and newer data on S0-2.
Another way to potentially reduce the mass regime even further is by estimating the Roche limit of the companion black hole.
Knowing stellar properties as their mass, radius and temperature will make it straight forward to determine a range the Roche limit can exist in, in the mass regime.

The maximum mass of the companion black hole corresponds to the mass of an IMBH, which is a type of black hole still under investigation. Their origin is not well known and if our galactic center resides a IMBH in orbit of Sgr. A* it will give rise to more questions than answers.
In 2030's LISA will be launched and then it will be possible to observe the center of the Milky Way and get a better understanding of IMBH and of what lurks in orbit of Sgr. A*.

References

[1] *The History of the Discovery of Sgr A**. Retrieved February 15, 2022 from
https://md64.medium.com/the-history-of-the-discovery-of-sgr-a-11b6658f8ab8

[2] Melia, F. (2007). *The Galactic Supermassive Black Hole* (pp. 2-5). Princeton
University Press

[3] Frolov, V. P. & Zelnikov, A. (2011). *Introduction to Black Hole Physics* (pp.
3-11, 36-40). Oxford University Press

[4] *"Supermassive Prime Time" – Unknown Objects Detected Orbiting Milky
Way's 'Lurking Monster'*. Retrieved October 19, 2021 from
https://dailygalaxy.com/2019/05/supermassive-prime-time-unknown-objects-detected

[5] *First Image of a Black Hole*. Retrieved January 17, 2022 from https://www.
eso.org/public/images/eso1907a/?lang

[6] *Scientific Background on the Nobel Prize in Physics 2020 - THEORET-
ICAL FOUNDATION FOR BLACK HOLES AND THE SUPERMASSIVE
COMPACT OBJECT AT THE GALACTIC CENTRE*. Retrieved September
21, 2021 from https://s3.eu-de.cloud-object-storage.appdomain.cloud/
kva-image-pdf/2021/10/sciback_fy_en_20.pdf

[7] Freedman, R.F, Geller, R. M & Kaufmann III, W.J. (2014). *Universe* (10th
ed.) (pp. 9, 96-97, 173, 339-340, 485, 603-625, 703-708). W.H. Freeman and
Company

[8] Carroll, B. W. & Ostlie, D. A. (2017). *An Introduction to Modern Astrophysics*
(2nd ed.) (pp. 27, 49, 60-63, 75-76, 633-646, 658-659, 723-724, 1015-1016). Cam-
bridge University Press.

[9] *Mass Chart for Dead Stars and Black Holes*. Retrieved February 8, 2022 from
https://www.nasa.gov/jpl/nustar/pia18842

[10] *What are intermediate-mass black holes?*. Retrieved Feburary 10, 2022 from
https://astronomy.com/news/2019/07/what-are-intermediate-mass-black-holes

[11] Guidry, M. (2019). *Modern General Relativity - Black Holes, Gravitational Waves, and Cosmology* (pp. 243, 281-284). Cambridge University Press

[12] Young, H. D & Freedman, R. A. (2016) *University Physics with Modern Physics* (14th global ed.) (pp. 435-437, 444). Pearson Education

[13] Ryden, B. & Peterson, B. M. 2021). *Foundations of Astrophysics* (pp.93-94, 480, 489-503). Cambridge University Press

[14] *What Does It Mean When A Black Hole Is Dormant?*. Retrieved October 19, 2021 from https://www.forbes.com/sites/quora/2016/02/29/what-does-it-mean-when-a-black-hole-is-dormant/?sh=1f1da6c033b4

[15] *The Beginning to the End of the Universe: How black holes die*. Retrieved February 8, 2022 from https://astronomy.com/magazine/news/2021/02/the-beginning-to-the-end-of-the-universe-how-black-holes-die

[16] Peterson, B. M. (1997). *An Introduction to Active Galactic Nuclei*. (pp 35). Cambridge University Press.

[17] *The Biggest Myth About Black Holes*. Retrieved February 15, 2022 from https://www.forbes.com/sites/startswithabang/2018/12/20/the-biggest-myth-about-black-holes/?sh=7c17dc9a6001

[18] Åkesson, A.T. & Kristensen. C.C. (2019) *Determination of the mass of Sagittarius A* from stellar orbits and an estimate of the Milky Way's lifetime as an active galaxy*. Bachelor thesis - Not published.
Link: https://www.dropbox.com/s/vi7eyg99vlm4apo/Bachelor%20Thesis-final.pdf?dl=0

[19] *Evolutionary channels of binary black holes: the impact of common envelope*. Retrieved February 10, 2022 from http://tesi.cab.unipd.it/63466/1/Spezzati_tesi.pdf

[20] Mapelli, M. (2020). *Binary Black Hole Mergers: Formation and Populations*. Frontiers in Astronomy and Space Sciences 7. doi: 10.3389/fspas.2020.00038

[21] *What happens when two supermassive black holes merge?*. Retrieved February 10, 2022 from https://www.esa.int/ESA_Multimedia/Images/2019/05/What_happens_when_two_supermassive_black_holes_merge

[22] *LIGO - Gravitational Waves*. Retrieved February 10, 2022 from https://www.ligo.caltech.edu/page/gravitational-waves

[23] *COSMOS Legacy Survey Shows Evidence of Intermediate-Mass Black Holes*. Retrieved September 21, 2021 from https://www.nasa.gov/mission_pages/chandra/images/cosmos-legacy-survey-shows-evidence-of-intermediate-mass-black-holes.html

[24] Abbott, R. et al. (2020). *GW190521: A Binary Black Hole Merger with a Total Mass of 150 $M_{\odot}$*. Physical Review Letters, 125(10). doi: https://doi.org/10.1103/PhysRevLett.125.101102

[25] *SEARCH FOR INTERMEDIATE MASS BLACK HOLE BINARIES IN THE FIRST AND SECOND OBSERVING RUNS OF THE ADVANCED LIGO AND VIRGO NETWORK*. Retrieved February 10, 2022 from https://www.ligo.org/science/Publication-O1O2IMBH/

[26] Greene, J. E. et al. (2020). *Intermediate-Mass Black Holes*. Annual Review of Astronomy and Astrophysics, 58(1). doi: 10.1146/annurev-astro-032620-021835

[27] *BH and NS Mass Chart*. Retrieved February 10, 2022 from https://www.ligo.caltech.edu/image/ligo20171016a?fbclid=IwAR0N3roZC2wYyZ9IJXcYOgujv0xZSmzlhQifmuJALsmakqC9vP9Za42VVjU

[28] Naoz, S. et al. (2020). *A HIDDEN FRIEND FOR THE GALACTIC CENTER BLACK HOLE, SGR A**. The Astrophysical Journal, 888(1). doi:10.3847/2041-8213/ab5e3b

[29] Naoz, S. (2016). *The Eccentric Kozai-Lidov Effect and Its Applications*. Annual Review of Astronomy and Astrophysics, 54(1). doi: 10.1146/annurev-astro-081915-023315

[30] Naoz, S. et al. (2013). *Resonant Post-Newtonian Eccentricity Excitation in Hierarchical Three-body Systems.* The Astrophysical Journal, 733(2). doi: 10.1088/0004-637X/773/2/187

[31] Naoz, S. & Li. G. et al. (2017). *THE ECCENTRIC KOZAI-LIDOV MECHANISM FOR OUTER TEST PARTICLE.* The Astrophysical Journal, 154(1). doi:10.3847/1538-3881/aa6fb0

[32] Peißker. F. et al. (2020a). *S62 on a 9.9-year orbit around SgrA*.* The Astrophysical Journal, 889(1). doi: 10.3847/1538-4357/ab5afd

[33] *Tapping into light's hidden information to push fundamental diffraction limit.* Retrieved February 25, 2022 from https://physicsworld.com/a/tapping-into-lights-hidden-information-to-push-fundamental-diffraction-limit/

[34] Chromey, F. R. (2010). *To Measure the Sky* (pp. 138-141, 180-183) Cambridge University Press

[35] *UCLA Galactic Center Group - Images.* Retrieved November 18, 2021 from http://www.astro.ucla.edu/~ghezgroup/gc/images.html

[36] Boehle, A. et al. (2016). *An Improved Distance and Mass Estimate for Sgr A* from a Multistar Orbit Analysis.* The Astrophysical Journal, 830(1). doi: 10.3847/0004-637x/830/1/17

[37] Schödel, R. et al. (2013). *Holographic imaging of crowded fields: high angular resolution imaging with excellent quality at very low cost.* Monthly Notices of the Royal Astronomical Society, 429(2). doi: 10.1093/mnras/sts420

[38] Ghez, A.M. et al. (2003). *Full Three Dimensional Orbits For Multiple Stars on Close Approaches to the Central Supermassive Black Hole.* Astronomische Nachrichten, 324(S1). doi: 10.1002/asna.200385103

[39] Ghez, A.M. et al. (2005). *Stellar Orbits around the Galactic Center Black Hole.* The Astrophysical Journal, 620(2). doi: 10.1086/427175

[40] Meyer, L. et al. (2012). *The Shortest Known Period Star Orbiting our Galaxy's Supermassive Black Hole*, 338(6103). doi:10.1126/science.1225506

70

[41] Abuter, R. et al. (2018). *Detection of the gravitational redshift in the orbit of the star S2 near the Galactic centre massive black hole*. Astronomy & Astrophysics, 615. doi: 10.1051/0004-6361/201833718

[42] Abuter, R. et al. (2019). *A geometric distance measurement to the Galactic Center black hole with 0.3% uncertainty*. Astronomy & Astrophysics, 625. doi:10.1051/0004-6361/201935656

[43] Harrison, W. & Goodrich, R. W. (1999). *The NIRC User's Manual*. Retrieved October 7, 2021 from https://www2.keck.hawaii.edu/inst/nirc/manual/Manual.html

[44] *W. M. Keck Observatory*. Retrived October 14, 2021 from https://keckobservatory.org/about/keck-observatory/

[45] *Keck I And Keck II Telescopes*. Retrived October 6, 2021 from https://keckobservatory.org/about/telescopes-instrumentation/

[46] *NIRC2 Home page*. Retrieved October 6, 2021 from https://www2.keck.hawaii.edu/inst/nirc2/

[47] *New Technology Telescope*. Retrieved October 14, 2021 from https://www.eso.org/public/teles-instr/lasilla/ntt/

[48] *The NTT enclosure*. Retrieved January 31, 2022 from https://www.eso.org/public/images/eso0912b/?lang

[49] *Max Planck Institute for Extraterrestrial Physics - SHARP*. Retrieved October 7, 2021 from https://www.mpe.mpg.de/ir/sharpi.

[50] *Introduction, SHARP2* Retrieved October 19, 2021 from https://www.mpe.mpg.de/resources/IR/sharp2+/manual/node2.html#SECTION00200000000000000000

[51] *Very Large Telescope: The world's most advanced visible-light astronomical observatory*. Retrieved October 14, 2021 from https://www.eso.org/public/teles-instr/paranal-observatory/vlt/

[52] *NACO: Nasmyth Adaptive Optics System (NAOS) – Near-Infrared Imager and Spectrograph (CONICA)*. Retrieved October 14, 2021 from https://www.eso.org/public/teles-instr/paranal-observatory/vlt/vlt-instr/naco/

[53] *GRAVITY*. Retrieved October 14, 2021 from https://www.eso.org/public/teles-instr/paranal-observatory/vlt/vlt-instr/gravity/

[54] *SINFONI: Spectrograph for INtegral Field Observations in the Near Infrared*. Retrieved October 14, 2021 from https://www.eso.org/public/teles-instr/paranal-observatory/vlt/vlt-instr/sinfoni/

[55] *Keck Observers' Newsletter*. Retrieved February 1, 2022 from https://www2.keck.hawaii.edu/inst/newsletters/Vol7/index.html

[56] Barlow, R.J. (1989) *Statistics: A Guide to the Use of Statistical Methods in the Physical Sciences* (pp. 83-84). Wiley

[57] Peißker, F. et al. (2020b) *S62 and S4711: Indications of a population of faint fast moving stars inside the S2 orbit S4711 on a 7.6 year orbit around Sgr A**. The Astrophysical Journal, 899(1). doi: 10.3847/1538-4357/ab9c1c

[58] Habibi, M. et al. (2017). *TWELVE YEARS OF SPECTROSCOPIC MONITORING IN THE GALACTIC CENTER: THE CLOSEST LOOK AT S-STARS NEAR THE BLACK HOLE*. The Astrophysical Journal, 847(2). doi: 10.3847/1538-4357/aa876f

[59] *LISA - Laser Interferometer Space Antenna*. Retrieved February 15, 2022 from https://lisa.nasa.gov/

A   Plots Used To Obtain Data

Plots used in Åkesson & Kristensen (2019) [18] in order to retrieve data.
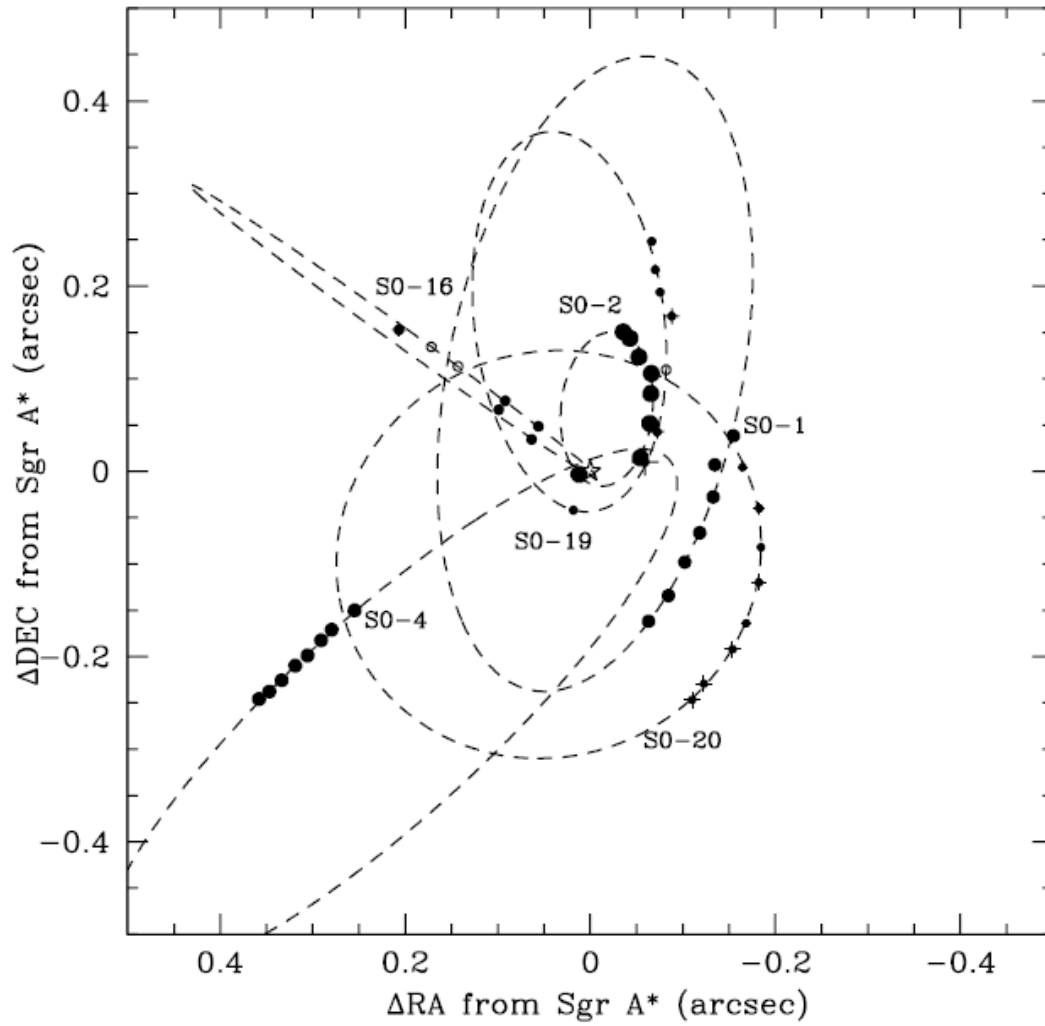

Figure 23: Ghez et al. (2003): The annual positions of 6 stars with orbital solutions. Figure 1b from Ghez et al. (2005) [38]
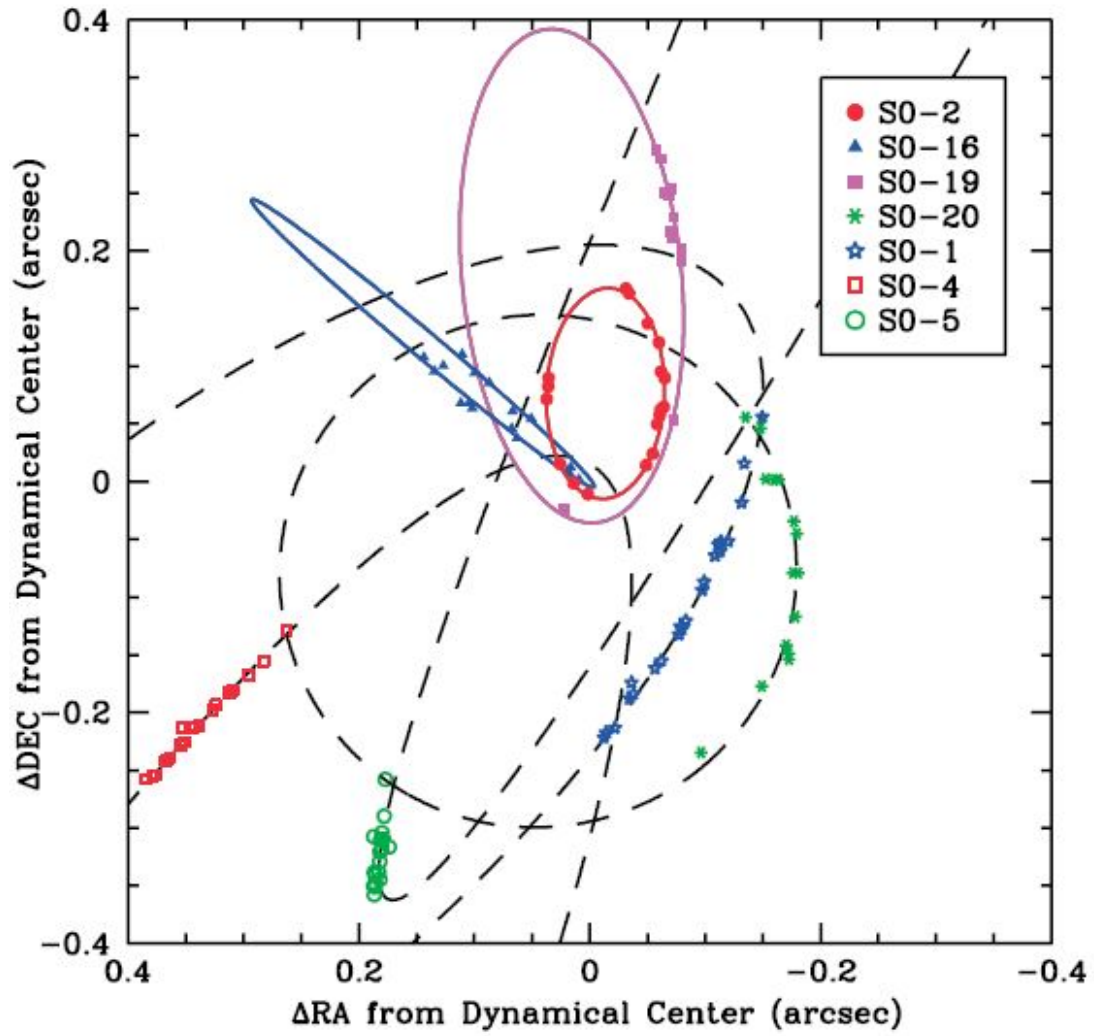
Figure 24: Ghez et al. (2005): Positions and orbital fits for seven of stars. The orbit of S0-1 differ from Ghez et al. (2003) due to changing the focus of the elliptical orbit compared to the position of Sgr A*. Figure 2 from Ghez et al. (2005) [39]
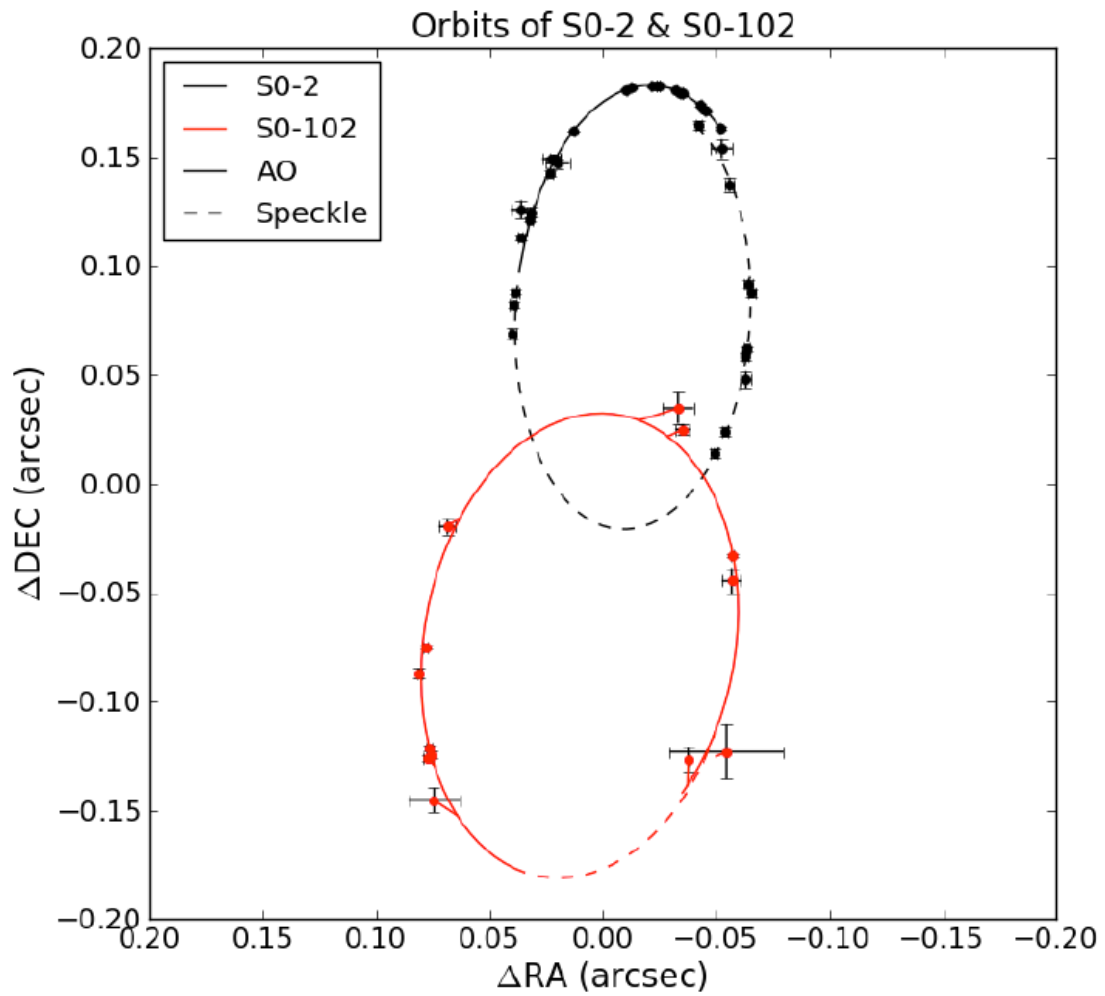
Figure 25: Meyer et al. (2012): Orbital fit of stars S0-2 (black) and S0-102 (red) showing their position. The dashed lines represent speckle data and the solid line represent A= observations. S0-2 data is obtained in the period 1995 to 2012, while S0-102 data is obtained from 2000 to 2012. Figure 2 from Meyer et al. (2012) [40]
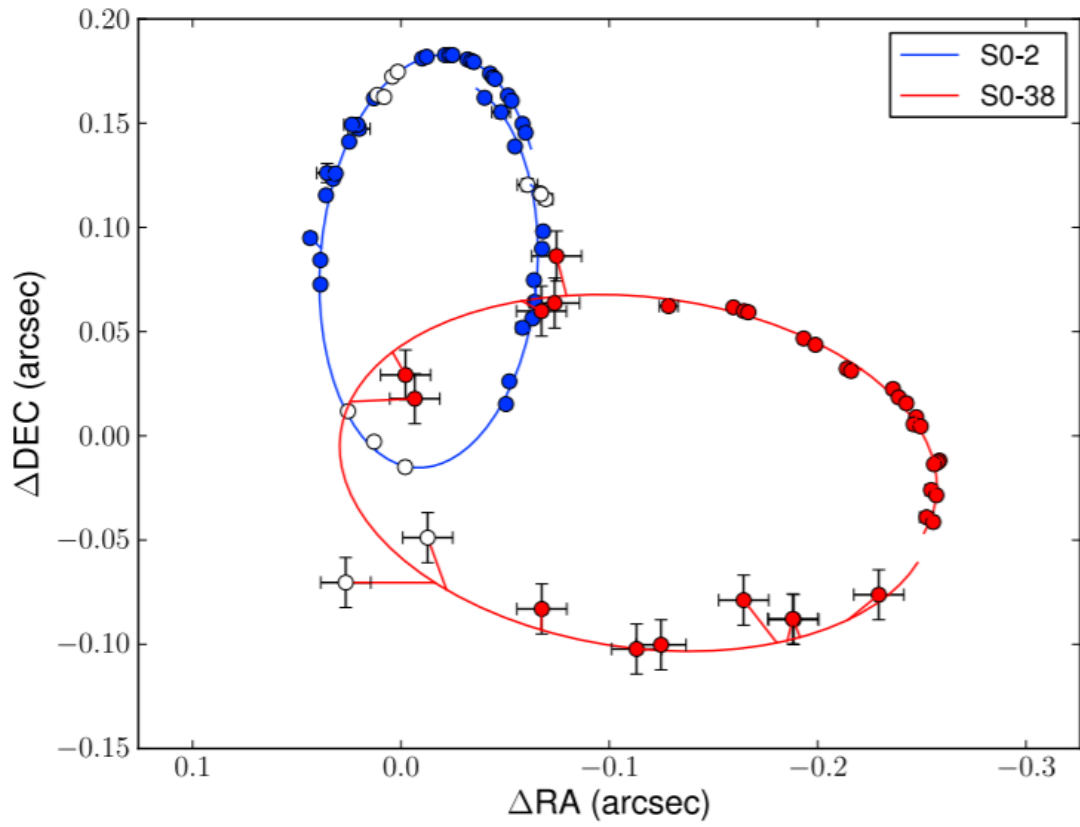
Figure 26: Boehle et al. (2016): Orbital fit of stars S0-2 (blue) and S0-38 (red) on the plane of the sky showing their position, obtained from 1995 to 2014. Figure 5 from Boehle et al. (2016) [36]
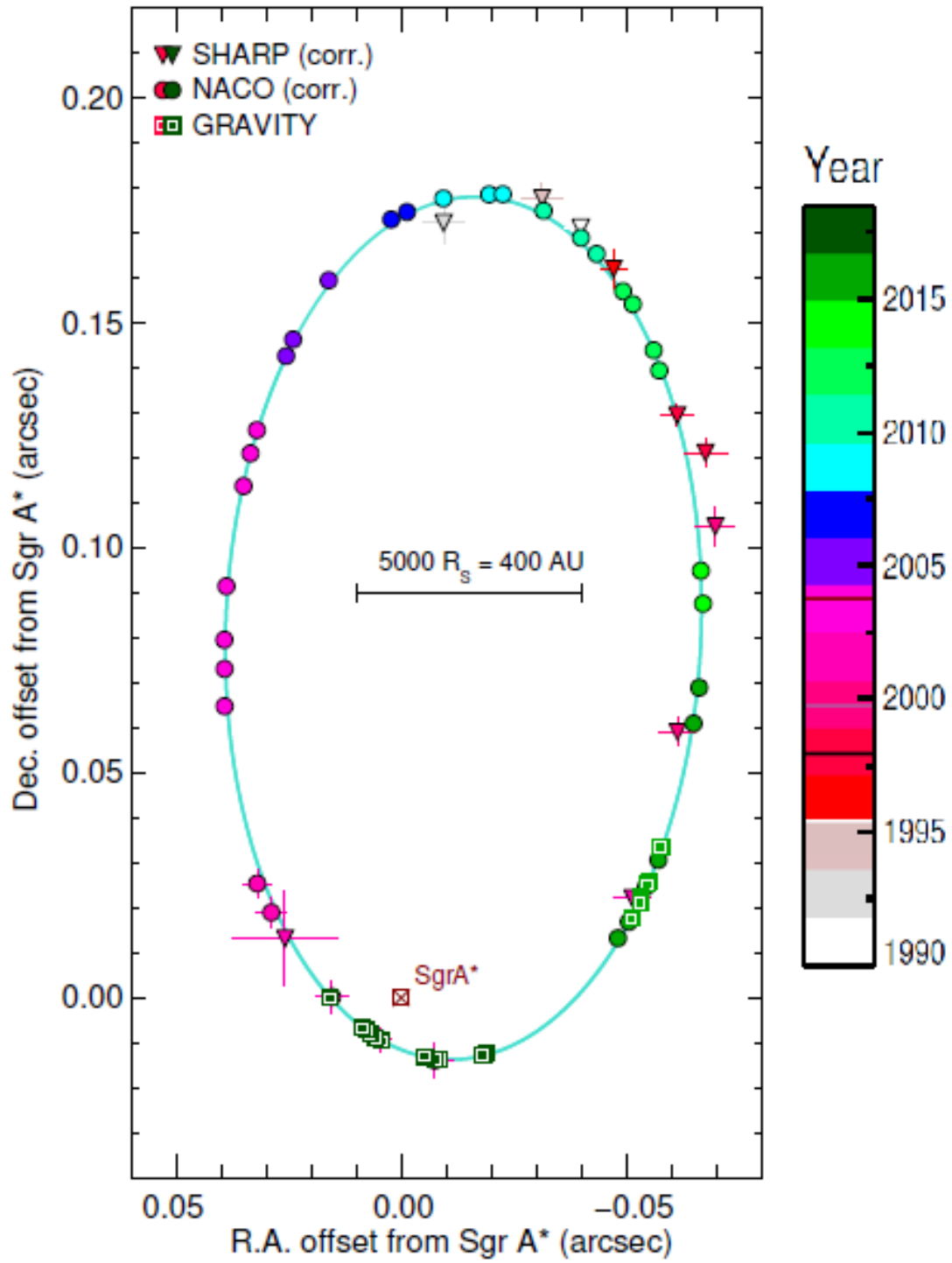
Figure 27: Abuter et al. (2018): Projected orbit of S0-2 relative to Sgr. A*. Data obtained from 1992 to 2018. Figure 2 from Abuter et al. 2018 [41]

B   Additional Plot

A plot of all the semi-major axis data of S0-2 from Åkesson & Kristensen (2019) have been plotted. This yields the same result as Figure 19.
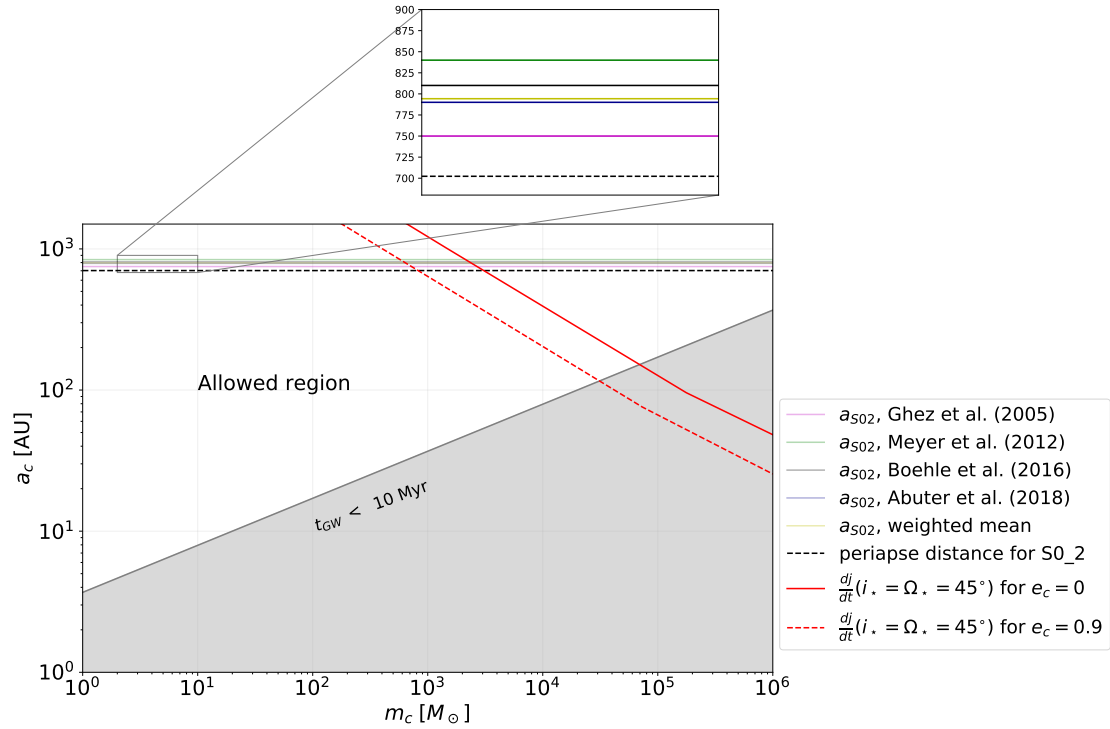
Figure 28: Results with data of S0-2 from Åkesson & Kristensen (2019). Plotted are the semi-major axis for the different stars, the timescale t_{GW} and dj/dt for $e_c = 0$ and $e_c = 0.9$

C   Results in Larger Scale

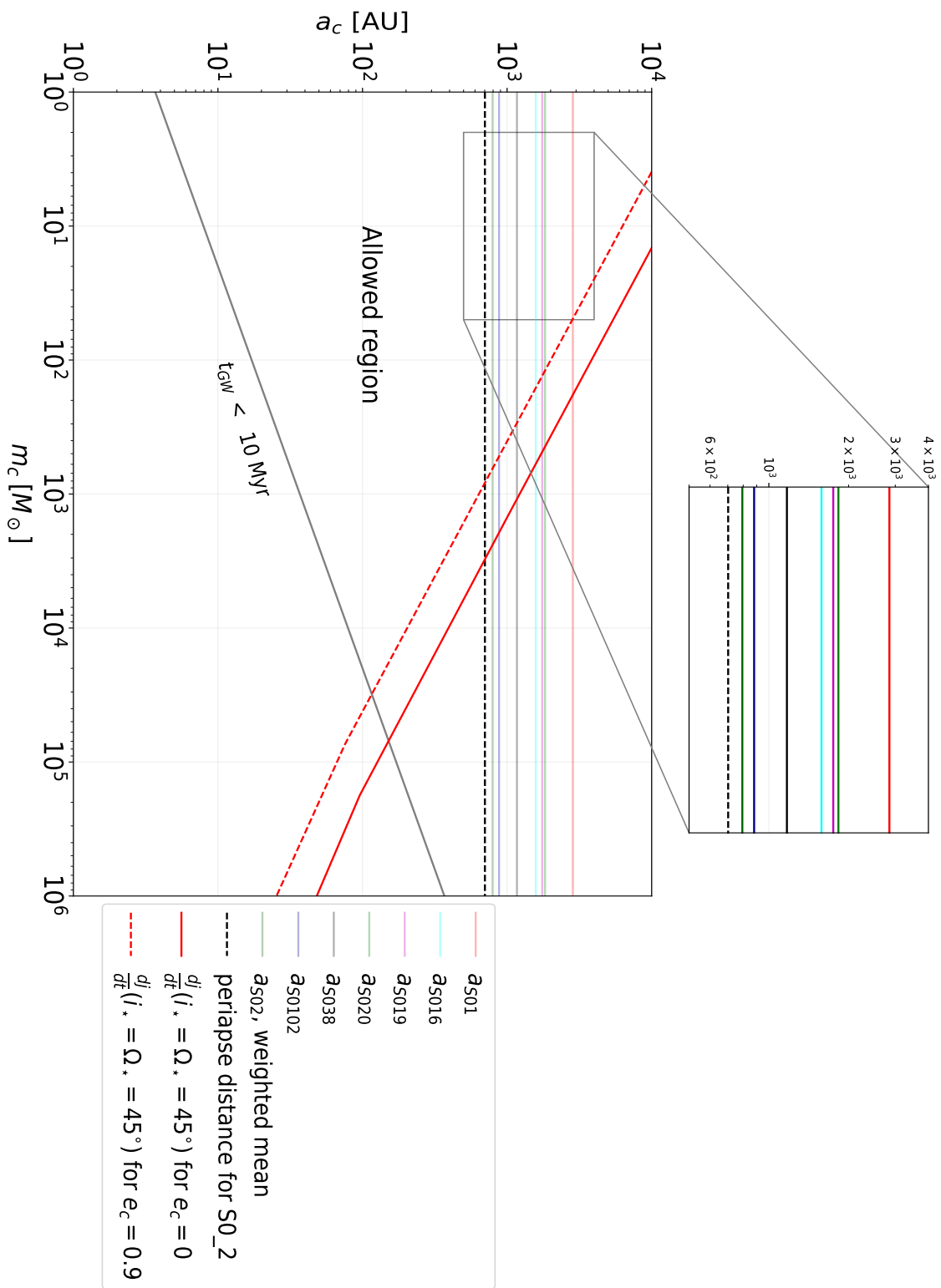In this section the results and the additional plot can be found in a larger and more readable size.

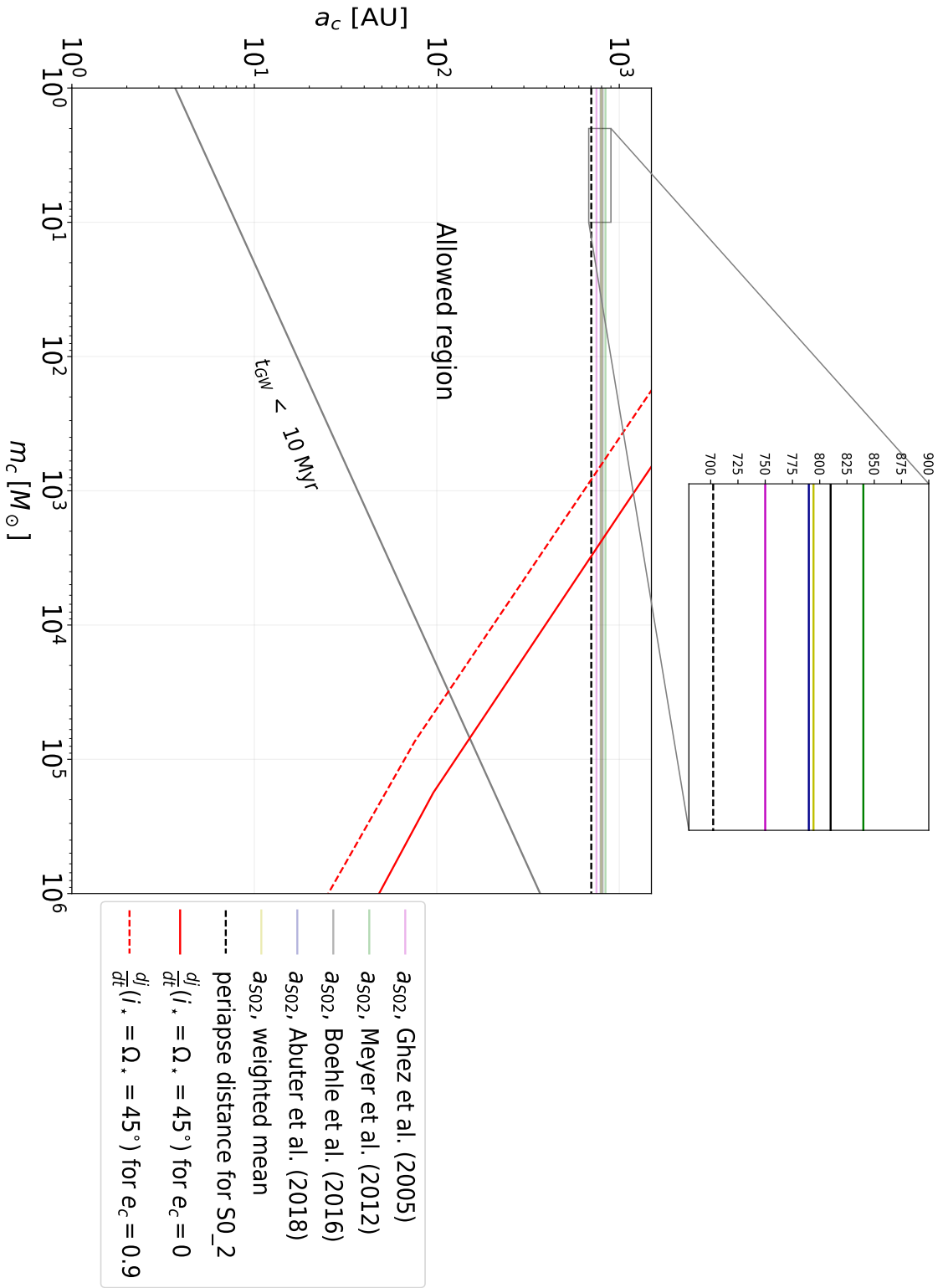Figure 29: Bigger size of figure 19
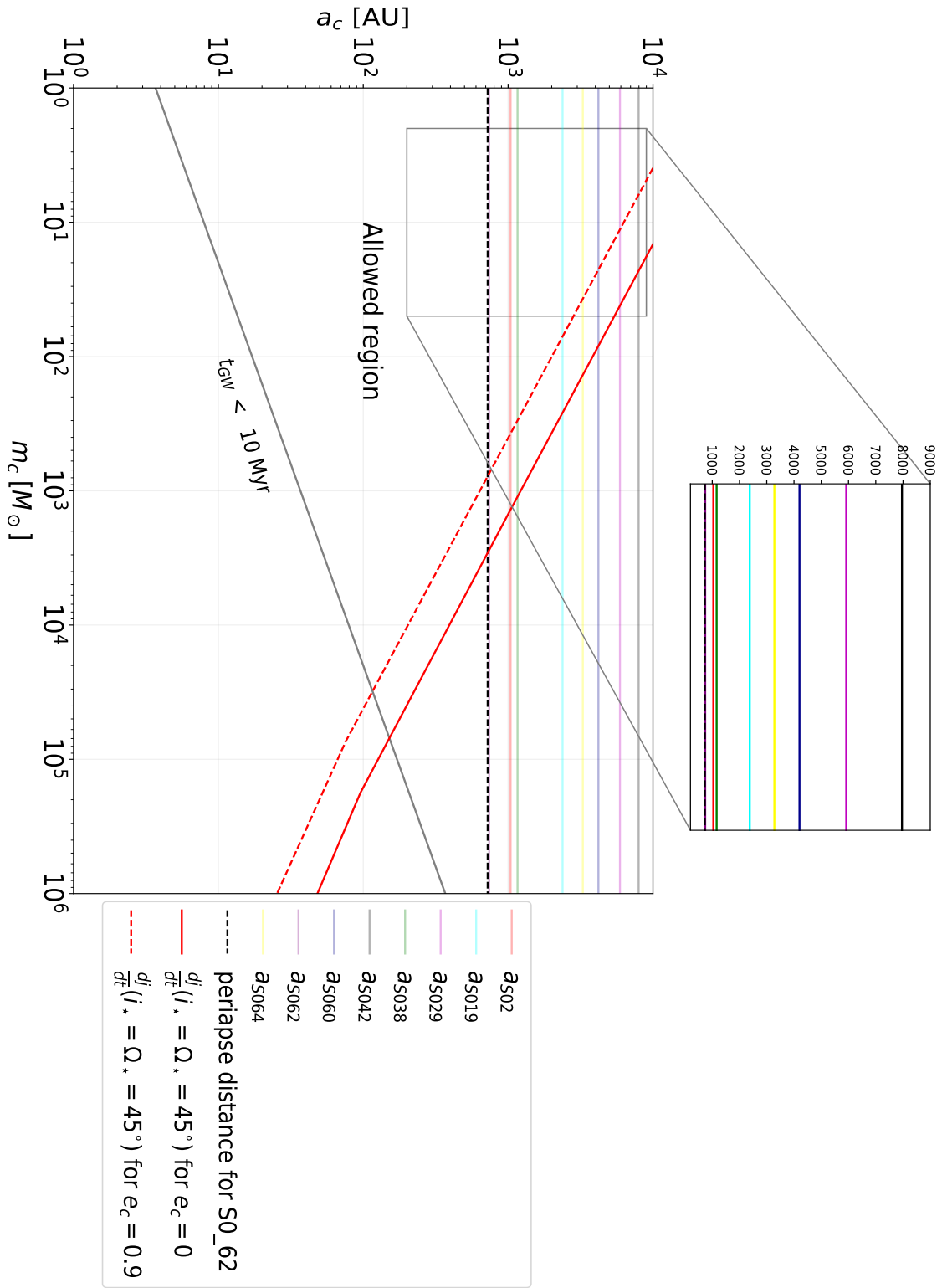
Figure 30: Bigger size of figure 28
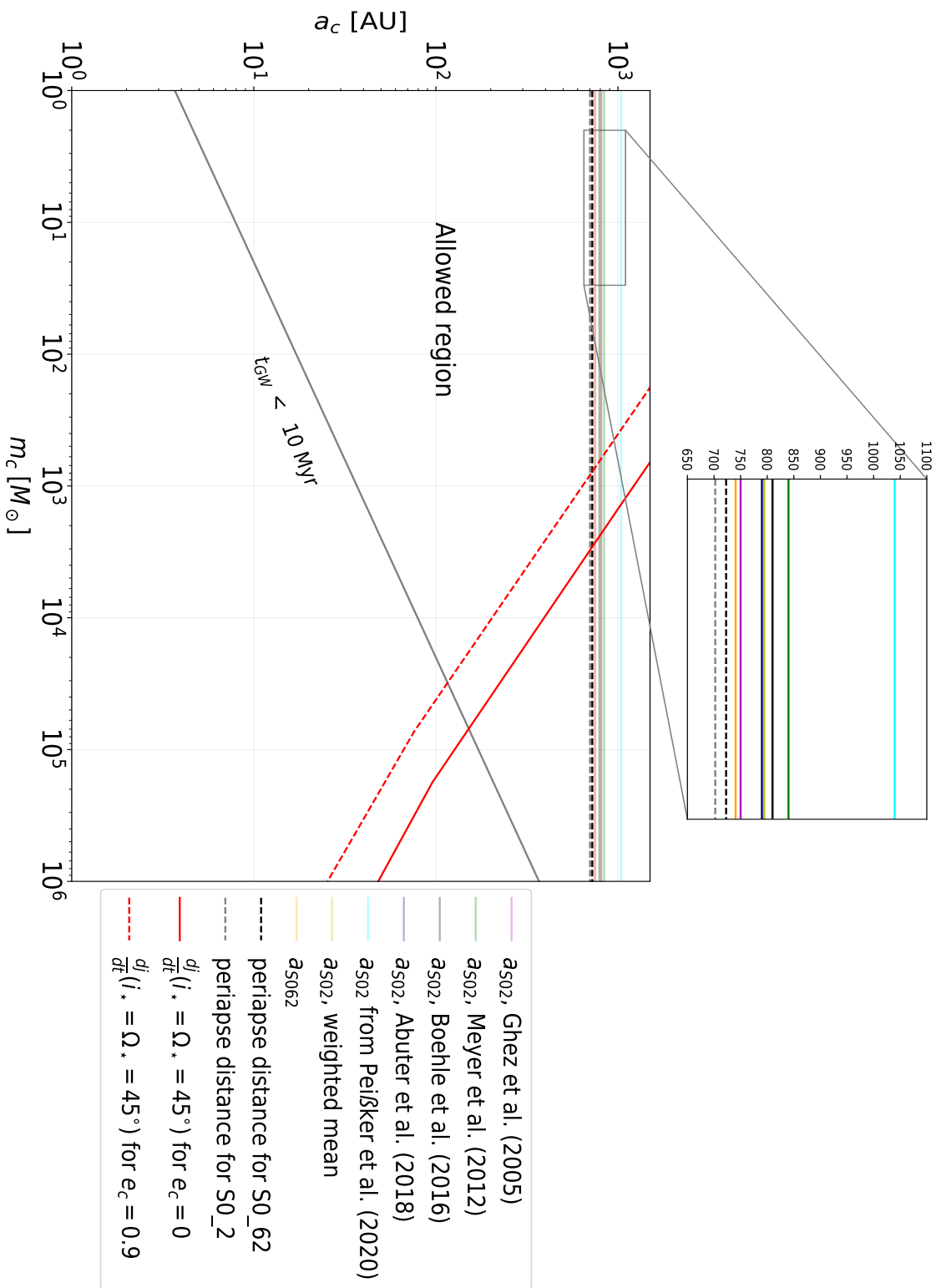
Figure 31: Bigger size of figure 20

Figure 32: Bigger size of figure 21

D Abbreviations

AGN: Active Galactive Nuclei

AO: Adaptive Optics

BH: Black Hole

EKL: Eccentric Konzai-Lidov

ESO: European Southern Observatory

GR: General Relativity/relativistic

GW: Gravitational Waves

iEKL: Inverse Eccentric Konzai-Lidov

IMBH: Intermediate-mass black hole

LGS: Laser Guide Star

LIGO: Laser Interferometer Gravitational-Wave Observatory

LISA: Laser Interferometer Space Antenna

NACO: Nasmyth Adaptive Optics System (NAOS) Near-Infrared Imager and Spectrograph (CONICA)

NGS: Natural Guide Star

NIR: Near Infrared

NIRC: Near Infrared Camera

NTT: New Technology Telescope

OSIRIS: (OH-Suppressing Infrared Imaging Spectrograph

PSF: Point-spread function

SAA: shift-and-add

Sgr.A*: Saggitarius A*

SMBH: Supermassive Black Hole

SPIFFI: SPectrometer for Infrared Faint Field Imaging

UTs: Unit Telescopes

VLT: Very Large Telescope

VLTI: ESO Very Large Telescope Interferometer